Interlocking Triplet Electronic States of Isocyanic Acid: Sources of Nonadiabatic Photofragmentation Dynamics†

Edward F. Valeev, Wesley D. Allen, and Henry F. Schaefer III*

Center for Computational Quantum Chemistry, University of Georgia, Athens, Georgia 30602

Attila G. Császár

Department of Theoretical Chemistry, Eötvös University, P.O. Box 32, H-1518 Budapest 112, Hungary

Allan L. L. East

Department of Chemistry, University of Regina, Regina, Saskatchewan, Canada SAS 0A2

Received: October 23, 2000

The triplet electronic states of isocyanic acid have been systematically investigated by means of state-of-the-art electronic structure methods, including various correlation techniques based on the coupled-cluster ansatz [CCSD, EOM-CCSD, CCSD(T), and BD(TQ)], second- through fifth-order Møller−Plesset perturbation theory (MP2-MP5), and the complete active space self-consistent field approach. The one-particle [(C,N,O)/H] basis sets for these studies ranged in quality from [4s2p1d/2s1p] to [7s6p5d4f3g2h1i/6s5p4d3f2g1h]. Vertical excitation energies were determined for the lowest 13 triplet states (5 valence, 8 Rydberg), and potential energy curves for bending to and from linearity were generated for 10 of these states, revealing intricate state interactions and numerous actual and avoided crossings. An extensive mapping was then executed for the interlocking $\tilde{a}^3A''$ and $\tilde{b}^3A'$ surfaces, which produced geometric structures, relative energies, harmonic vibrational frequencies, and selected large-amplitude vibrational eigenstates, for torsional conformers, inversion barriers, fragmentation barriers, dissociation products, and ionization limits, in addition to identifying intermingled conical intersections. The lowest-energy conformer on the $\tilde{a}^3A''$ surface is actually a skewed (C_1) structure with a torsion angle of 143°, a barrier to planarity of only 74 cm^{-1}, an adiabatic excitation energy near $T_0 =$ 30 056 cm^{-1}, and an exit barrier for $^3NH + CO$ fragmentation of only about $\Delta E_0^* = 3252$ cm^{-1}. It is discovered that there are actually no legitimate minima (removed from conical intersections) on the $\tilde{b}^3A'$ surface, because in-plane optimizations bring associated structures below the companion $^3A''$ state and subsequently connect them to the lowest triplet surface via torsional excursions along imaginary-frequency normal modes.

I. Introduction

Isocyanic acid (HNCO) is among the family of CHNO compounds (and their simple salts) that played an important role in the early development of chemistry, beginning in the sixteenth century.[1] It is thus fitting that this fascinating species has become in the past few decades first a paragon of the rich spectroscopy of quasilinear molecules with large-amplitude vibrational motion[2,3] and then very recently a prototype of intricate photodissociation dynamics on a nexus of competing potential energy surfaces. In particular, isocyanic acid is among the few molecules of such limited size having chemically distinct dissociation processes effectively competing in the region of the first UV absorption band and yielding varied photolysis products, all of whose rovibrational state distributions can be interrogated in detail by modern laser techniques. Since the pioneering UV absorption work of Dixon and Kirby in 1968,[4] photochemical and related investigations[5−39] of HNCO have seemingly become legion, and several theoretical studies[3,40−47] have complemented and elucidated the experimental observations.

The prominent $S_0(^1A') \rightarrow S_1(^1A'')$ transition in HNCO results from a $2a'' \rightarrow 10a'$ electronic excitation, which engenders a sizable 0.2 Å elongation of the N−C bond and a prodigious bending of the N−C−O framework from 172° to near 125°.[3,43−46] While poor Franck−Condon overlap has precluded direct observation of the S_1 band origin, vibrationally mediated photofragment yield spectroscopy and multiphoton fluorescence spectroscopy have been employed within the past year[39] to pinpoint almost 70 excited vibrational states on the S_1 surface and to infer an adiabatic excitation energy of 32 449 ± 20 cm^{-1} via extrapolation of the anharmonic profiles. After $S_0 \rightarrow S_1$ photoexcitation, the following dissociation channels can be accessed:

$$HNCO(T_1) \rightarrow NH(X^3\Sigma^-) + CO(X^1\Sigma^+) \qquad D_0(S_0) = 30060 \pm 25\ cm^{-1} \quad (1)$$

$$HNCO(S_0, S_1, T_1, T_2) \rightarrow H(^2S) + NCO(\tilde{X}^2\Pi) \qquad D_0(S_0) = 38370 \pm 30\ cm^{-1} \quad (2)$$

$$HNCO(S_0, S_1) \rightarrow NH(a^1\Delta) + CO(X^1\Sigma^+) \qquad D_0(S_0) = 42750 \pm 25\ cm^{-1} \quad (3)$$

where the product thresholds [$D_0(S_0)$] with respect to the ground

† Part of the special issue "William H. Miller Festschrift".

* Corresponding author.

10.1021/jp0039114 CCC: $20.00
Published on Web 03/07/2001

state are the most recent values derived from both photofragment yield spectroscopy of jet-cooled HNCO and fits to the velocity distributions of photofragment ion images.[23,38]

At low excitation energies, isocyanic acid fragmentation can occur only via the ^{3}NH channel (1). The observed isotropy of the associated CO product angular distributions[38] suggests that the initially prepared S_1 state decays to an intermediate whose lifetime exceeds 5 ps before reaching T_1, as opposed to direct $S_1 \rightarrow T_1$ coupling, whose spin−orbit matrix elements are computed to be relatively small.[44] The most likely dissociation route is thus $S_1 \rightarrow S_0 \rightarrow T_1$, i.e., internal conversion (IC) followed by intersystem crossing (ISC) and subsequent triplet fragmentation. The efficacy of the $S_0 \rightarrow T_1$ process is demonstrated in the pyrolysis of HNCO(S_0), which is primarily initiated by ^{3}NH + CO formation.[42,48] The proposed three-step mechanism for channel (1) is also supported by various observations[23,32,38] just above the threshold for channel (2); specifically, the energy dependence of the relative product yields, similar state-specific effects in the yield spectra, and the isotropies of product recoil are all consistent with a common S_0 precursor for both dissociations. Channel (1) remains competitive at least up to 46 000 cm^{-1},[32,33] but the features that control the dynamics on the T_1 surface in various energy regimes are not fully characterized. For example, the exit barrier for ^{3}NH + CO formation has been predicted to lie near 5 kcal mol^{-1} by B3LYP[41] and CASPT2[44] computations with modest basis sets, but a definitive value is not known from either theory or experiment.

The intricacies of HNCO photodissociation greatly increase upon opening of the H + NCO channel, because the asymptotes are connected to four separate electronic surfaces [(S_0, S_1, T_1, T_2) in eq 2], remarkably all of which are accessible in the Franck−Condon region of photoexcitation. On the S_0 surface there is no barrier to H + NCO fragmentation, and thus at lower energies channel (2) selectively follows the S_0 route after internal conversion from S_1, giving statistical NCO product rotational distributions.[38] There is general agreement that on the S_1 surface H + NCO formation is blocked until energies well above the channel (3) threshold are reached, but there is wide discord among the various empirical[22,38] and theoretical[43−46] estimates of the relevant barrier heights. Both cis and trans fragmentation cols appear to exist, with the former transition state lying lower by at least 4000 cm^{-1}.[43,44,46] Based on the angular isotropy of H-atom signals in channel (2), an experimental lower limit of 8140 cm^{-1} has recently been surmised for the barrier to direct dissociation on S_1. In contrast, recent CASPT2 and MRCI computations have placed this (cis) barrier at 3950,[44] 4500,[46] and 6050 cm^{-1}.[43] With regard to the T_1 and T_2 surfaces for channel (2), there exist theoretical predictions[41,44] for cis and trans transition states similar in quality and character to their S_1 counterparts, but no information has been gleaned from photodissociation experiments.

The final layer of complexity in the multistate photodissociation dynamics of HNCO is encountered when the ^{1}NH channel (3) becomes operative. Once again, the S_0 surface exhibits no barrier for fragmentation, and ^{1}NH products are thus detected at thermochemical threshold. However, with increasing energy, direct dissociation on the competing S_1 surface quickly dominates, as evidenced by a sharp rise in the overall yield of channel (3) at the expense of channel (2), and a rapid linewidth broadening in the ^{1}NH yield spectrum.[17,19,21,23−25,30,33,34] Photofragment ion imaging reveals a nearly isotropic product recoil distribution for channel (3) at 43 161 cm^{-1} but high anisotropy at 43 274 cm^{-1}, indicating a change to direct, impulsive dynamics in this interval and suggesting a small barrier of 470 ± 60 cm^{-1} on the S_1 surface.[38] In this case there is nice accord with the aforementioned CASPT2 and MRCI studies,[43−46] which predicted fragmentation transition states that are highly trans-bent, have N−C distances near 2 Å, and lie 350−700 cm^{-1} above the ^{1}NH + CO asymptotes. The occurrence of impulsive dissociation dynamics once sufficient energy is available in channel (3) is indeed anticipated from the geometric changes that attend the $S_0 \rightarrow S_1$ excitation (vide supra), as transitions in the Franck−Condon region prepare the S_1 state with a highly compressed N−C bond and a large driving force for N−C−O bending. Numerous recent experiments[7−10,14,15,18,19,24−26,31] have probed the resulting rotational, vibrational, and translational product state distributions in channels (2) and (3) throughout the 193−260 nm photolysis range in search of dynamical signatures. For example, at 217.6 nm a majority of the available energy in channel (3) is released as translation ($f_{trans} = 0.6$), CO is produced rotationally hot with some vibrational excitation ($f_{rot,CO} = 0.26$, $f_{vib,CO} = 0.06$), but ^{1}NH appears rotationally cold due to dynamical constraints ($f_{rot,NH} = 0.07$).[31] At 260 nm in channel (2), translational energy release once again dominates ($f_{trans} = 0.66$), yet the impulsive dynamics also yield a large degree of bending vibrational excitation in the NCO fragment ($f_{bend} = 0.24$).[19]

A number of innovative experiments by the Crim group[17,20,22,27−29,36,37] on vibrationally mediated photodissociation (VMP) of HNCO in channels (2) and (3) have heightened general interest in this system, challenged prevailing qualitative dynamical models, and unravelled detailed couplings in the vibrational spectroscopy of the ground electronic state. In one of the best current examples of bond-selective chemistry,[20] the quantum yield of NCO at a total photolysis energy of 44 440 cm^{-1} was enhanced from 0.22 to 0.83 by initial state-specific excitation of the N−H stretch in its $3\nu_1$ overtone, thus changing the preferred course of photodissociation from channel (3) to channel (2). More recently, initial vibrational excitation of $3\nu_1$ was found to decrease the fractional photolysis yield of ^{1}NH relative to ^{3}NH by a factor of approximately two compared to the isoenergetic photodissociation of a thermal sample of HNCO, a nonadiabatic phenomenon observed at both 43 480 and 44 440 cm^{-1}.[36] The explanation of these dynamics in the context of the abundant data for non-VMP processes hinges on an understanding of how various (coupled) vibrational modes promote either direct dissociation on the S_1 surface, internal conversion to S_0, or intersystem crossing to nearby triplet surfaces, or perhaps some mixture of these processes.[20,22,32,33,36,38,39,43,44] Klossika and co-workers[45−47] have begun an ambitious project toward this end by constructing a five-dimensional MRCI surface in a spline representation for the S_1 state and performing classical trajectory calculations for the direct ^{1}NH + CO dissociation. Very recently, Kaledin et al.[44] have investigated more directly the role of internal conversion and intersystem crossing in HNCO photodissociation by computing CASSCF equilibrium geometries, transition states, minima on seams of surface crossings, and nonadiabatic coupling matrix elements for the (S_0, S_1, T_1, T_2) manifold. These ab initio studies constitute important first steps toward quantitative theoretical treatments of the tangled dynamics in channels (1), (2), and (3).

The arduous pursuit of mastery of the photochemistry of isocyanic acid will undoubtedly continue for years to come, not merely for establishing HNCO as a paradigm of multistate quantum dynamics but also due to the intriguing rovibrational spectroscopy of this quasilinear molecule, its presence in galactic radiation sources, and the practical importance of HNCO

combustion chemistry.[3] Indeed, isocyanic acid, as a source of NH radicals, is the centerpiece of the RAPRENO$_x$ process[3,49] for the removal of NO$_x$ combustion products from exhaust streams, and it is of interest in fuel-N conversion in flames;[48,50−52] moreover, HNCO is an early product of the decomposition of RDX and HMX explosives.[52,53] In this paper we renew earlier efforts[3] toward the full characterization and development of potential energy surfaces for the low-lying electronic states of HNCO by invoking high-level coupled-cluster methods (inter alia) with very large basis sets in pursuit of improved (subchemical) accuracy. To limit the study to digestible proportions, we focus here on exploration and mapping of the triplet states of this molecule, which have thus far received meager attention in ab initio investigations of HNCO excited states. We start by determining vertical excitation energies for 13 triplet states and following the bending potentials for 10 of them to and from linearity. An extensive mapping is then performed of the salient features of the interlocking $\tilde{a}^3A''$ and $\tilde{b}^3A'$ surfaces. Our intent is to sustain and elevate the synergy between theory and experiment, which has heretofore been so fruitful in discovering and elucidating the photofragmentation dynamics of HNCO.

II. Theoretical Methods

The atomic-orbital Gaussian basis sets employed in this study are denoted as DZ(d,p), TZ(2d1f,2p1d), PBS, PBS++spd, and cc-pV*X*Z (X = D,T,Q,5,6), ranging from 47 to 511 contracted functions for HNCO. The DZ(d,p) basis[54,55] is of double-ζ plus polarization quality and is identical to that used in earlier investigations by some of us on HNCO.[3] The TZ(2d1f,2p1d) basis is comprised of Huzinaga−Dunning[54,56] (C,N,O) (10s6p/5s3p) and (unscaled) H(5s/3s) contractions augmented with correlation-optimized (2d1f) and (2s1p) polarization manifolds, respectively.[57] The polarized basis set (PBS) of Sadlej[58,59] is a compact (C,N,O) (10s6p4d/5s3p2d) and H(6s4p/4s2p) set designed specifically for studies on excited electronic states having some Rydberg character. Nonetheless, as for ketene,[60] description of higher-lying Rydberg states of HNCO requires even more diffuse functions, and thus in some work the PBS basis was augmented with two sets of even-tempered diffuse s, p, and d functions centered near the molecular center of mass, specifically at the carbon nucleus. Several variants of the resulting PBS++spd basis, including a larger one with diffuse functions added on all atoms and a smaller (PBS++s) set with no pd augmentation, were also employed in exploratory and confirmatory computations. The most extensive computations in this study were performed with the cc-pV*X*Z family of correlation-consistent basis sets,[57,61,62] whose contracted Gaussian orbitals for [(C,N,O)/H] extend from (DZ) [3s2p1d/2s1p] to (6Z) [7s6p5d4f3g2h1i/6s5p4d3f2g1h]. In all cases except DZ(d,p), only pure spherical harmonics of the polarization manifolds were included in the basis sets.

Reference electronic wave functions were determined by the single-configuration, self-consistent field, restricted and unrestricted Hartree−Fock [R(O)HF and UHF] methods,[63−66] and by the complete active space self-consistent field (CASSCF) approach.[67] The CASSCF procedures involved an (8,6) active space of eight electrons in six orbitals, constituting the valence π space when HNCO is linear. Dynamical electron correlation was accounted for by configuration interaction including all single and double excitations (CISD),[68−70] by Møller−Plesset perturbation theory carried out from second through fifth order (MP2-MP5),[64,66,71−74] by the coupled cluster singles and doubles method (CCSD),[75−79] by CCSD theory augmented with a perturbative contribution from connected triple excitations,[80,81] and by the Brueckner doubles method (BD)[82,83] with analogous corrections for both triple and quadruple excitations [BD(TQ)].[74] For all open-shell states, the Møller−Plesset methods were implemented consistently with UHF reference wave functions. In mapping and characterizing stationary points of the two lowest triplet states of HNCO, open-shell coupled-cluster energies and gradients were generally determined by application of the usual spin−orbital formalism of the theory with (semicanonical) restricted orbitals [RCCSD and RCCSD(T)].[84−87] In contrast, final energetic predictions for the adiabatic excitation energy and fragmentation barrier of $\tilde{a}^3A''$ HNCO employed coupled-cluster wave functions built from unrestricted orbitals [UCCSD, UCCSD(T), and UBD(TQ)]. In these cases, the spin contamination in the UHF reference wave function is only in the 0.07−0.08 range, which is easily overcome by the high-order correlation treatments. Extensive investigation of the triplet eigenspectrum of HNCO was achieved by the EOM-CCSD method[88] while ionized limits of the system were probed via its EOMIP-CCSD variant.[89−92] In the determination of optimum geometric structures and harmonic vibrational frequencies, the correlation treatments included all orbitals in the active space for technical reasons. However, series of single-point computations were subsequently executed in which the 1s core orbitals were frozen, and in all DZ(d,p) CISD results a 1s occupied/1s* virtual pair of orbitals was kept inactive for each heavy atom. Finally, for some crucial energetic quantities, core-correlation shifts were evaluated via all-electron computations with the cc-pCVTZ basis,[93] which, unlike its cc-pVTZ counterpart, is designed to reliably recover such effects.

Geometric structures of the different electronic states of HNCO were optimized to better than 10^{-4} Å and 0.01° using analytic gradient[94] techniques at the RHF, CASSCF, CISD, RCCSD,[85] RCCSD(T),[86] and EOM-CCSD[95,96] levels of theory. Quadratic force constants for harmonic vibrational frequency analyses were obtained via analytic second derivatives[94] for RHF and CASSCF wave functions, but in all other cases force fields were determined by numerical differentiation of analytic first derivatives.

The accuracy of the EOM-CCSD method for an excited electronic state depends strongly on the characteristic level of excitation: high accuracy can be expected only for singly excited states. However, this criterion was met easily here, as measured by the approximate excitation level (AEL) proposed by Stanton and Bartlett,[88] which was found to be smaller than 1.08 for all triplet states of HNCO considered. In addition, multireference deficiencies in the RCCSD and RCCSD(T) methods do not seem to be of particular concern for the nonlinear structures on the $\tilde{a}^3A''$ and $\tilde{b}^3A'$ surfaces reported here, because the computed T_1 amplitudes and estimates[97] of a common T_1 diagnostic[98,99] never exceeded 0.181 and 0.0241, respectively.

Basis set extrapolations, an integral feature of the focal-point analysis method[40,100,101] for inferring ab initio limits, utilized the asymptotic formulas $E_X = E_{CBS} + a\exp(-bX)$ and $E_X = E_{CBS} + aX^{-3}$ for Hartree−Fock and correlation energies, respectively, where X is taken as the cardinal number of the cc-pV*X*Z series and CBS denotes the complete basis set limit. Extrapolations of the MP series to estimate full configuration interaction (FCI) limits employed shifted [2,1] Padé approximants with data up to fifth order.[100]

All electronic structure computations were performed with various implementations of the program packages ACESII,[102] PSI,[103] and Gaussian 94.[104] Absolute total energies for focal-point analyses and quadratic force constant matrices for selected

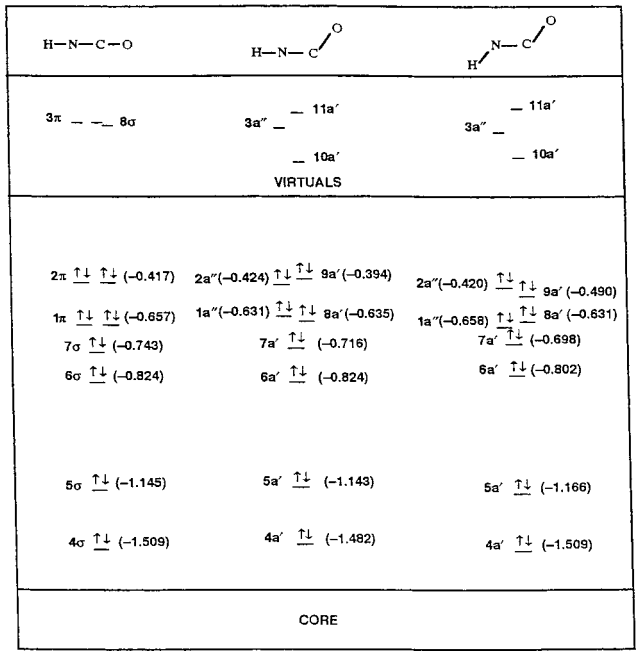

Figure 1. Variation of the low-lying DZ(d,p) RHF canonical orbital energies for ground-state HNCO with respect to in-plane bending distortions. The final geometry (far right) is the optimum DZ(d,p) RHF structure of the anti conformer of $\tilde{a}^3A''$ HNCO. The preceding structures are obtained by sequentially straightening out θ(H−N−C) and ρ(N−C−O) with the $\tilde{a}^3A''$ bond distances fixed.

stationary structures are available as supplementary material. See ref 105 for access information.

III. Characterization of the Triplet Eigenspectrum

The nature of the low-lying triplet electronic states of HNCO is revealed by the orbital energy diagram in Figure 1 for linear HNCO and structures generated therefrom by successive N−C−O and H−N−C bending. Further elucidation can be achieved by constructing analogous diagrams for the isoelectronic species CO_2,[106] NCO^-,[5] and H_2CCO[60] and perusing the extensive spectroscopic[107−109] and theoretical literature for these molecules. The 2π HOMO of linear HNCO lies over 50 000 cm^{-1} above the next lowest orbital and is thus the origin of at least the first 10 excited triplet states. The lowest-lying valence states arise from $2\pi \rightarrow 3\pi$ single excitations, which give rise to a ($^3\Sigma^+$, $^3\Delta$, $^3\Sigma^-$) triplet manifold and companion singlet states, each zeroth-order triplet wave function involving a $\pm 2^{-1/2}$ superposition of two equivalent determinants of $(2\pi_{x;y})^2(2\pi_{y;x})^1(3\pi_{[x,y];[x,y]})^1$ type. Both the EOM-CCSD and CASSCF(8,6) methods correctly produce pure angular momentum states for the valence ($^3\Sigma^+$, $^3\Delta$, $^3\Sigma^-$) manifold, yielding the predictions collected in Table 1. In the optimum ($^3\Sigma^+$, $^3\Delta$, $^3\Sigma^-$) structures, both the C−O and N−C bond lengths are 0.06−0.08 Å longer than in the ground state, whereas the N−H distance is contracted by about 0.012 Å. These changes are reflected in expected ω_i shifts in opposite directions, particularly large (> 600 cm^{-1}) reductions in the antisymmetric stretching frequencies (ω_2). Both theoretical methods agree on the state ordering within the manifold, but the preferred, dynamically correlated EOM-CCSD approach gives larger splittings: $\Delta E_e(^3\Delta - {}^3\Sigma^+) = 4733$ cm^{-1} and $\Delta E_e(^3\Sigma^- - {}^3\Sigma^+) = 7822$ cm^{-1}. The cluster of states begins near $T_e = 55\,000$ cm^{-1}, or in the vicinity of 24 500 cm^{-1} above the anti conformer of the $\tilde{a}^3A''$ state (vide infra). By comparison, the valence ($^3\Sigma_u^+$, $^3\Delta_u$, $^3\Sigma_u^-$) manifold of CO_2 exhibits the same state ordering and comparable splittings but lies roughly 10 000 cm^{-1} higher in excitation energy.[106]

The bending potentials issuing from the ($^3\Sigma^+$, $^3\Delta$, $^3\Sigma^-$) linear states are governed by both qualitative Mulliken−Walsh arguments[110,111] and mathematical features of the Renner effect.[112] As shown in Figure 1, N−C−O bending is driven by massive 3π ($10a'$) stabilization, while subsequent H−N−C bending is engendered by a 2π ($9a'$) lowering which localizes a lone pair on nitrogen. Accordingly, all harmonic bending frequencies for the linear triplet states in Table 1 are imaginary, with sizable magnitudes, except for ω_5 of the $^3\Sigma^-$ state at the PBS EOM-CCSD level, which is disturbed by a strong second-order Jahn−Teller interaction (as described in footnote *c* of the table). In Renner−Teller systems, the potential energy surface of states that are doubly degenerate at linearity must ultimately split into two components upon bending; however, states of angular momentum Λ will not have differing force constants until order 2Λ.[113] Therefore, the two $^3\Delta$ components of HNCO must have the same bending harmonics (unlike the commonly encountered case of Π states), as confirmed by the data reported in Table 1.

An extensive EOM-CCSD accounting of the bending potentials of the 10 lowest triplet states of isocyanic acid is summarized in Figure 2. For vertical excitations of linear HNCO, a $^3\Pi$ state of ($2\pi \rightarrow 3s$) Rydberg character appears at the lower end of the valence ($^3\Sigma^+$, $^3\Delta$, $^3\Sigma^-$) cluster. In contrast, at the ($^3\Sigma^+$, $^3\Delta$, $^3\Sigma^-$) optimum structure in Table 1, the $^3\Pi$ state lies respectively (5605, 1001, 1993) cm^{-1} (above, above, below) the corresponding valence-state position at the PBS EOM-CCSD level. A similarity thus exists with the eigenspectrum of CO_2,[106] in which a $^3\Pi_u$ Rydberg state lies between the second and third members of the valence ($^3\Sigma_u^+$, $^3\Delta_u$, $^3\Sigma_u^-$) manifold at optimum valence excited-state geometries, albeit with a larger $^3\Pi_u - {}^3\Delta_u$ separation. Upon EOM-CCSD optimization of the lowest $^3\Pi$(R) state of HNCO under linearity constraints, we observed a monotonic decay to H(^2S) + NCO($^2\Pi$) fragments lying some 20 000 cm^{-1} lower in energy, indicating that this state is unstable toward dissociation.

The bending potential curves in Figure 2 exhibit no less than five actual intersections (1 V−V, 2 V−R, 2 R−R) and four avoided crossings (3 V−R, 1 R−R), the most significant being the valence−valence $\tilde{a}^3A''/\tilde{b}^3A'$ intersection near 136°, and the valence−Rydberg $\tilde{a}^3A''/\tilde{c}^3A''$ avoided crossing in the vicinity of 150°. An analogue of the $\tilde{a}^3A''/\tilde{b}^3A'$ intersection is not present in CO_2, where the lowest triplet state ($^3B_2$) correlates directly to $^3\Sigma_u^+$ at linearity while its $^3A_2$ counterpart remains at least 0.5 eV higher in energy.[106] In the EOM-CCSD curves of HNCO, the [$^3\Sigma^+$(V), $^3\Pi$(R), $^3\Delta$(V), $^3\Sigma^-$(V)] linear states are connected diabatically to the [$\tilde{b}^3A'$, ($\tilde{e}^3A'$, $\tilde{c}^3A''$), ($\tilde{d}^3A'$, $\tilde{a}^3A''$), $\tilde{f}^3A''$] states in C_s symmetry. As mentioned above, the $^3\Delta$(V) state drops slightly below $^3\Pi$(R) upon optimization, whence the $^3\Delta \rightarrow \tilde{a}^3A''$ correlation properly becomes adiabatic for nonvertical excitations, an important point for mapping the $\tilde{a}^3A''$ surface for in-plane distortions (section IV).

In Table 2 vertical excitation energies from the equilibrium structure of $\tilde{X}^1A'$ HNCO are listed for 13 triplet and 6 ionized states. The qualitative assignments of the predicted transitions are based on computed EOM-CCSD natural orbitals, the spatial extent of the excited state as measured by $\langle r^2 \rangle$, comparison of results from the extended PBS and PBS++spd sets versus the valence-restricted cc-pVTZ basis, and the quantum defects[107−109,112] of the Rydberg states [$\delta = 1.23-1.27$ for the s states ($\tilde{c}$, $\tilde{e}$, $\tilde{k}$), and $\delta = 0.48-0.78$ for the p states ($\tilde{g}$, $\tilde{h}$, $\tilde{\imath}$, $\tilde{\jmath}$, $\tilde{m}$)]. Positions of additional higher-lying

TABLE 1: Characterization of the Linear Triplet States of HNCO within the Lowest $\pi \rightarrow \pi^*$ Manifold[a]

	$\tilde{X}^1A'$	$^3\Sigma^+$	$^3\Delta$	$^3\Sigma^-$
r_e(C−O)	1.1718 (1.1621)	1.2468 (1.2295)	1.2508 (1.2373)	1.2544 (1.2446)
r_e(N−C)	1.2297 (1.2148)	1.2900 (1.2872)	1.2880 (1.2909)	1.2883 (1.2943)
r_e(N−H)	1.0153 (0.9956)	1.0031 (0.9846)	1.0023 (0.9841)	1.0029 (0.9837)
θ_e(H−N−C)	120.08 (125.54)	180 (180)	180 (180)	180 (180)
ρ_e(N−C−O)	172.59 (170.65)	180 (180)	180 (180)	180 (180)
ΔE_e	−29881 (−29694)	24568 (30377)	29301 (33026)	32390 (35302)
T_e	0 (0)	54449 (60071)	59182 (62720)	62271 (64996)
ω_1 NH stretch	3675 (3937)	3832 (4089)	3846 (4098)	3838 (4103)
ω_2 NCO anti stretch	2314 (2478)	1762 (1688)	1670 (1534)	1591 (1386)
ω_3 NCO sym stretch	1317 (1391)	1141 (1209)	1133 (1190)	1122 (1174)
$\omega_4(\pi)$ HNC bend	*b*	1437*i* (1232*i*)	1356*i* (1154*i*)	1136*i* (1115*i*)
$\omega_5(\pi)$ NCO bend	*b*	1089*i* (889*i*)	3040*i* (1072*i*)[c]	2233 (1253*i*)[c]

[a] All-electron PBS EOM-CCSD [DZ(d,p) CASSCF(8,6)] optimum geometric parameters [r_e(Å); ρ_e and θ_e(deg)] and harmonic vibrational frequencies [ω_i(cm^{-1})] for the lowest $\pi \rightarrow \pi^*$ triplet manifold are compared to analogous values for the ground electronic state. Corresponding energies (ΔE_e) relative to the $\tilde{a}^3A''$ anti conformer and adiabatic excitation energies (T_e) are listed in cm^{-1}, as given by single-point frozen-core computations. The all-electron (frozen-core) PBS CCSD and DZ(d,p) CASSCF(8,6) total energies for the $\tilde{X}^1A'$ state are −168.346 845 (−168.300 365) and −167.876 897 E_h, respectively. [b] PBS EOM-CCSD [DZ(d,p) CASSCF(8,6)] bending frequencies for the nonlinear, planar (C_s) equilibrium structure of the $\tilde{X}^1A'$ state: $\omega_4(a') = 868$ (827), $\omega_5(a') = 563$ (582), $\omega_6(a'') = 629$ (610) cm^{-1}. [c] In the PBS EOM-CCSD eigenspectrum, the ($2\pi \rightarrow 3s$) $^3\Pi$ state nestles between the $^3\Delta$ and $^3\Sigma^-$ states, a feature which is unaccounted for by the valence-π CASSCF(8,6) method. Strong state repulsions along the ω_5 mode give rise to a second-order Jahn−Teller effect which drives the N−C−O bending potential substantially down and up for the $^3\Delta$ and $^3\Sigma^-$ states, respectively.

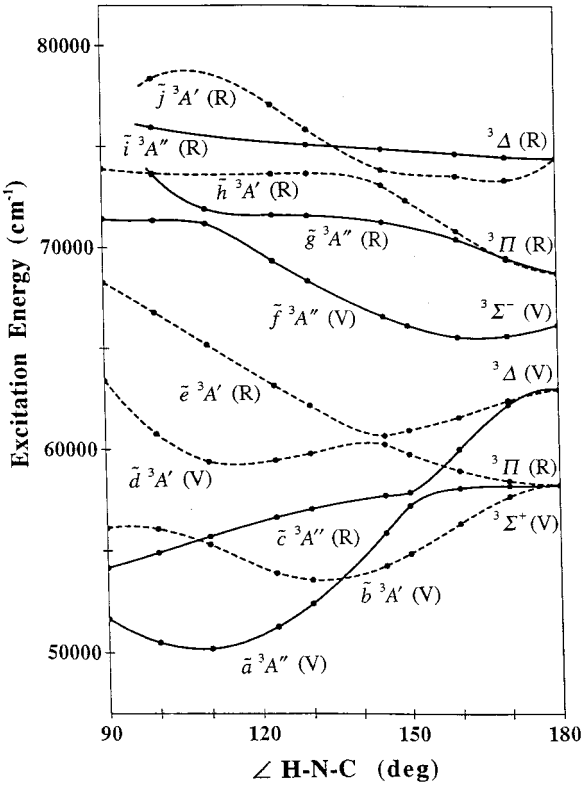

Figure 2. PBS EOM-CCSD potential energy curves for H−N−C bending of the 10 lowest triplet electronic states of HNCO. The (all electron) energy points were obtained at planar structures determined by fixing ∠(H−N−C) and optimizing the remaining 4 degrees of freedom for the ground electronic state. Accordingly, the plotted excitation energies are referenced to the $\tilde{X}^1A'$ optimum (all electron) PBS CCSD structure and total energy given in Table 1 and footnote *a* therein. Solid (dashed) lines indicate $^3A''$($^3A'$) curves; (V,R) designations for the linear and bent term symbols signify (valence−Rydberg) character.

members of the $9a' \rightarrow ns$ and $2a'' \rightarrow ns$ Rydberg series may readily be estimated from the Rydberg formula, $E_n = E_\infty - 109737\ (n-\delta)^{-2}$, with a quantum defect of about 1.25. The reliability of the (PBS, PBS++spd) EOM-CCSD vertical triplet eigenspectrum is bolstered by nice accord with several UV absorptions for corresponding singlet transitions[108] and with the available experimental data[16,114−117] on HNCO ionization potentials (see footnotes *e* and *f* of Table 2). Moreover, numerous EOM-CCSD applications, including studies on the isoelectronic ketene molecule,[60] suggest an expected accuracy for these predictions of 1000 cm^{-1} or better. An important conclusion from Table 2 is that all vertical excitation energies lie well above the three lowest dissociation asymptotes, $D_0(^3\text{NH}+\text{CO}) = 30\,060 \pm 25$ cm^{-1},[38] $D_0(\text{H}+\text{NCO}) = 38\,370 \pm 30$ cm^{-1},[23] and $D_0(^1\text{NH}+\text{CO}) = 42\,750 \pm 25$ cm^{-1}.[38]

IV. The $\tilde{a}^3A''$ Surface

An extensive mapping and characterization of the potential energy surface of the valence $\tilde{a}^3A''$ state of HNCO was undertaken at several levels of theory. Stationary structures and harmonic vibrational frequencies for torsional conformers, inversion barriers, fragmentation barriers, dissociation products, and the lowest ionization limit are compiled in Tables 3 and 4. Focus should be directed to the complete set of data listed for our highest level of theory [cc-pVTZ RCCSD(T)], although comparisons with predictions from other methods prove instructive.

Molecular bending from the optimum $^3\Delta$(V) linear structure (Table 1) affords almost a 30 000 cm^{-1} reduction in the energy of the $\tilde{a}^3A''$ component, consistent with the aforementioned orbital energy considerations. The lowest triplet state becomes ($2a'' \rightarrow 10a'$) in electronic character, with (C−O, N−C, N−H) distances elongated about (0.02, 0.2, 0.02) Å compared to the ground state (cf. Table 2, foonote *a*), thus evidencing N−C/C=O single/double bonds. Moreover, the vibrational coupling between the bond angles, which is pronounced in the ground state,[3] is broken in the $\tilde{a}^3A''$ state, leading to widely separated ω_4 and ω_5 values in Table 4. A reference point is provided by trans-bent, planar structure **A**, i.e., the conformer termed anti in Table 3, whose bond angles ρ_e(N−C−O) and θ_e(H−N−C) are predicted to lie near 125.3° and 106.5°, respectively. The torsional potential ensuing from the anti conformer is quite sensitive to the level of theory. With the DZ(d,p) RHF method, the anti conformer is a low-energy minimum, equivalent gauche minima at $\tau = \pm 57°$ appear 135 cm^{-1} higher, and the corresponding syn structure constitutes a 442 cm^{-1} barrier for gauche interconversion. This uncorrelated energy profile suggests a naive picture of internal rotations about an N−C single bond that are mediated by repulsions between the CO moiety and electrons arrayed about an sp^3-hybridized nitrogen atom.

TABLE 2: Vertical Triplet Excitation Energies (cm^{-1}) for $\tilde{X}^1A'$ HNCO[a]

			vertical excitation energy (EOM-CCSD)[d]		
state	description[b]	$\langle r^2\rangle$[c]	PBS	cc-pVTZ	PBS++spd
$\tilde{b}\ ^3A'$ HNCO	V ($9a' \rightarrow 10a'$)[e]	127	53 928	54 352	53 920
$\tilde{d}\ ^3A'$	V ($2a'' \rightarrow 3a''$)[e]	127	59 492	59 953	59 467
$\tilde{e}\ ^3A'$	R ($9a' \rightarrow 3s$)[e]	146	63 127	70 490	63 055
$\tilde{h}\ ^3A'$	R ($2a'' \rightarrow 3p$)[e]	180	73 612		71 689
$\tilde{j}\ ^3A'$	R ($9a' \rightarrow 3p$)[e]	170	77 037		76 088
$\tilde{l}\ ^3A'$	V ($8a' \rightarrow 10a'$)	144	79 514	80 198	79 354
$\tilde{m}\ ^3A'$	R ($9a' \rightarrow 3p$)	188	80 207		78 171
$\tilde{A}\ ^2A'$ $HNCO^+$	V ($9a' \rightarrow \infty$)[f]		98 353		98 373
$\tilde{B}\ ^2A'$	V ($8a' \rightarrow \infty$)[f]		129 163		129 188
$\tilde{D}\ ^2A'$	V ($7a' \rightarrow \infty$)[f]		141 930		141 949
$\tilde{E}\ ^2A'$	V ($6a' \rightarrow \infty$)		164 319		164 345
$\tilde{a}\ ^3A''$ HNCO	V ($2a'' \rightarrow 10a'$)[e]	128	51 275	51 867	51 267
$\tilde{c}\ ^3A''$	R ($2a'' \rightarrow 3s$)	146	56 631	63 901	56 580
$\tilde{f}\ ^3A''$	V ($9a' \rightarrow 3a''$)	131	69 350	69 962	69 252
$\tilde{g}\ ^3A''$	R ($2a'' \rightarrow 3p$)[e]	170	71 585		70 644
$\tilde{i}\ ^3A''$	R ($2a'' \rightarrow 3p$)	167			75 097
$\tilde{k}\ ^3A''$	R ($2a'' \rightarrow 4s$)	259			77 717
$\tilde{X}\ ^2A''$ $HNCO^+$	V ($2a'' \rightarrow \infty$)[f]		92 378		92 408
$\tilde{C}\ ^2A''$	V ($1a'' \rightarrow \infty$)[f]		129 990		130 017

[a] Frozen-core energies evaluated at the unfrozen-core cc-pVTZ CCSD(T) ground-state optimum geometry: r_e(C−O) = 1.1668 Å, r_e(N−C) = 1.2165 Å, r_e(N−H) = 1.0027 Å, ρ_e(N−C−O) = 172.27°, θ_e(H−N−C) = 123.13°. [b] Each upper electronic state is labeled valence (V) or Rydberg (R) in character and is assigned to a single electronic excitation according to its EOM-CCSD natural orbitals. [c] Spatial extent (in $bohr^2$) of upper electronic state about the molecular center of mass, as given by the PBS++spd EOM-CCSD method. The analogous value for $\tilde{X}^1A'$ HNCO is 127 $bohr^2$. [d] Relative to the frozen-core ground-state total energies −168.299 853 (PBS), −168.403 857 (cc-pVTZ), and −168.300 951 (PBS++spd) E_h. [e] Comparative vertical excitation energies (cm^{-1}) for corresponding singlet transitions in the UV absorption spectrum of HNCO (ref 108): (50000, 52600, 59900) for the V[($9a'$, $2a''$) → ($10a'$, $3a''$)] manifold; 64100 for R($9a' \rightarrow 3s$); and (72930, 78000) among the R[($9a'$, $2a''$) → 3p] transitions. [f] Results collected from 3 sources indicate that the first four bands in the experimental photoelectron spectrum (refs 114, 16, and 116) of HNCO occur at 93520 ± 40 cm^{-1} ($2a'' \rightarrow \infty$, adiabatic), 99930 ± 850 cm^{-1} ($9a' \rightarrow \infty$, vertical), 125340 ± 400 cm^{-1} ($1a'' \rightarrow \infty$, adiabatic), which may include ionizations from a second, nearly degenerate orbital, and ca. 141000 cm^{-1} ($7a' \rightarrow \infty$, vertical).

Upon inclusion of dynamical electron correlation, the anti conformer becomes a transition state connecting shallow, equivalent skewed (trans C_1) minima. In the [DZ(d,p) CISD, cc-pVTZ RCCSD(T)] predictions, the extent of skewing is (24.96°, 37.24°), resulting in diminutive energy lowerings of (5, 74) cm^{-1}. The syn structure retains a Hessian index of 1 in the dynamically correlated treatments, but the syn−anti difference is more than twice the RHF value, specifically 1385 cm^{-1} in the cc-pVTZ CCSD(T) case. The gauche minima were found to concomitantly vanish. To demonstrate this point, a full probe of the torsional potential of $\tilde{a}^3A''$ HNCO was executed at the cc-pVTZ RHF, UMP2, RCCSD, and RCCSD(T) levels of theory, as shown in Figure 3 and detailed in its caption. The shallow RHF gauche minima become mere shoulders on the anti → syn ascent with the coupled-cluster methods. Note that UMP2 theory greatly overestimates this correlation effect, exaggerating the skewing and well depths of the C_1 minima and eradicating the gauche features completely. In summary, in the best predictions the $\tilde{a}^3A''$ state displays equivalent skewed minima and gauche shoulders, connected by anti and syn transition states, quite unlike the analogous $^1A''$ state, which appears to have relatively deep minima at both anti and syn conformations.[43,44]

In previous work from the Morokuma group[41] on $\tilde{a}^3A''$ HNCO torsional conformers, the 6-311G(d,p) B3LYP density-functional approach was found to yield both skewed ($\tau = \pm 135.8°$) and gauche ($\tau = \pm 61.1°$) minima, while the anti and syn structures both appear as transition states. The nonlocal hybrid exchange potential of B3LYP may be implicated for the spurious gauche minima, which are supported by Hartree−Fock theory. While the B3LYP syn−anti separation (3.8 kcal mol^{-1}) is close to the more reliable CCSD(T) values presented here, the predicted 44.2° twisting and 140 cm^{-1} drop of the skewed form vis-à-vis the anti reference point appears to be a significant overestimation. Our cc-pVTZ RCCSD(T) predictions also supersede additional $\tilde{a}^3A''$ HNCO results[44] at the CASPT2 level with a DZ(d,p)+diffuse basis set, which characterized the syn structure as a genuine minimum lying over 2000 cm^{-1} above equivalent skewed ($\tau = \pm 137°$) conformers.

The cc-pVTZ RCCSD(T) torsional potential of the $\tilde{a}^3A''$ state of HNCO depicted in Figure 3 possesses intricate structure which supports a fascinating, highly anharmonic vibrational eigenspectrum. Because the harmonic torsional frequency of the skewed minimum (ω_6 = 195 cm^{-1}, Table 4) is almost three times the skewed → anti barrier height, the question arises as to whether a bound eigenstate even exists below the barrier to planarity. By evaluating the $G(\tau,\tau)$ matrix element along the torsional path, constructing an interpolating function for the cc-pVTZ RCCSD(T) potential, and invoking the Cooley−Numerov procedure[118,119] for determining the exact torsional eigenstates, the following 17 energy levels (relative to the anti reference point) were found with the aid of the *Mathematica* package:[120,121] ϵ_τ = {−9, 52, 173, 269, 353, 438, 539, 655, 779, 914, 1041, 1201, 1296, 1517, 1552, 1869, 1876} cm^{-1}. Therefore, the ground vibrational level dips just below the electronic energy of the planar, anti configuration, while the anharmonic, zero-point energy for the torsional mode of the skewed minimum is 65 cm^{-1}, as opposed to 98 cm^{-1} in the harmonic approximation. A total of 13 torsional states lie below the syn barrier at 1385 cm^{-1}. The presence of the gauche shoulder is manifested as a minimum in the energy level spacings in the vicinity of the fourth torsional eigenvalue at 269 cm^{-1}.

Conformational interconversions on the $\tilde{a}^3A''$ surface can also be effected by both N−C−O and H−N−C inversions. To elucidate these transformation routes, the two-dimensional linear bending surface for planar $\tilde{a}^3A''$ HNCO, as depicted in Figure 4, was investigated. In the figure, the signed linear bending coordinates α(N−C−O) and β(H−N−C) are employed rather than their unsigned valence angle counterparts ρ(N−C−O) and θ(N−C−O) to reveal the full topography of the surface and

TABLE 3: Stationary Points on the $\tilde{a}^3A''$ Surface of Isocyanic Acid[a]

	E	ΔE_e	r_e(C−O)	r_e(N−C)	r_e(N−H)	ρ_e(N−C−O)	θ_e(H−N−C)	τ_e(H−N−C−O)	Hessian index[b]
Torsional Conformers									
anti (C_s) (**A**)									
DZ(d,p) RHF	−167.692 225	0	1.1624	1.4255	1.0114	127.11	108.04	180	0
DZ(d,p) CASSCF(8.6)	−167.741 601	0	1.190	1.401	1.011	125.2	108.3	180	0
DZ(d,p) CISD[c]	−168.088 483	0	1.1835	1.4397	1.0250	125.44	106.41	180	1
PBS EOM-CCSD	−168.164 216	0	1.1936	1.4111	1.0340	125.82	107.03	180	
PBS RCCSD	−168.174 427	0	1.1917	1.4356	1.0356	124.80	106.45	180	
PBS UCCSD	−168.173 954	0	1.1963	1.4236	1.0426	129.15	104.62	180	
TZ(2d1f,2p1d) RCCSD	−168.271 112	0	1.1781	1.4215	1.0232	125.45	106.77	180	1
cc-pVTZ RCCSD(T)	−168.295 614	0	1.1893	1.4130	1.0230	125.34	106.51	180	1
syn (C_s) (**C**)									
DZ(d,p) RHF	−167.689 594	577	1.1668	1.4171	1.0164	130.14	106.61	0	1
DZ(d,p) CASSCF(8,6)	−167.737 137	980	1.190	1.404	1.015	128.7	107.5	0	1
DZ(d,p) CISD[c]	−168.083 183	1163	1.1874	1.4287	1.0304	129.28	105.00	0	1
PBS EOM-CCSD	−168.157 084	1565	1.1984	1.3880	1.0438	131.35	105.41	0	1
TZ(2d1f,2p1d) RCCSD	−168.265 338	1267	1.1818	1.4092	1.0306	129.57	105.53	0	
cc-pVTZ RCCSD(T)	−168.289 304	1385	1.1924	1.4018	1.0309	129.71	105.37	0	1
skewed (trans C_1)									
DZ(d,p) CISD[c]	−168.088 508	−5	1.1837	1.4378	1.0252	124.60	106.45	155.04	0
cc-pVTZ RCCSD(T)	−168.295 953	−74	1.1907	1.4072	1.0231	123.14	106.93	142.76	0
gauche (cis C_1)									
DZ(d,p) RHF	−167.691 611	135	1.1651	1.4124	1.0140	125.82	109.02	56.94	0
Inversion Barriers									
ρ[anti → syn] (C_s) (**D**)									
DZ(d,p) RHF	−167.609 328	18194	1.1873	1.3832	1.0190	178.08	110.22	180	1
TZ(2d1f,2p1d) RCCSD	−168.194 994	16706	1.2065	1.3518	1.0447	177.10	110.83	180	1
cc-pVTZ RCCSD(T)	−168.219 932	16610	1.2192	1.3431	1.0484	176.81	111.08	180	1
θ[anti → syn] (C_s) (**B**)									
DZ(d,p) RHF	−167.639 149	11649	1.1686	1.3686	0.9903	130.89	179.96	180	1
TZ(2d1f,2p1d) RCCSD	−168.220 172	11180	1.1951	1.3403	1.0004	130.31	179.03	180	*d*
cc-pVTZ RCCSD(T)	−168.244 830	11146	1.2122	1.3265	0.9991	130.29	179.07	180	*d*
Fragmentation Barriers									
trans (C_s)									
DZ(d,p) RHF	−167.674 954	3791	1.1348	1.7188	1.0174	121.51	103.06	180	1
DZ(d,p) CISD[c]	−168.073 194	3356	1.1512	1.7971	1.0330	120.73	100.31	180	1
TZ(2d1f,2p1d) RCCSD	−168.257 498	2988	1.1394	1.8334	1.0321	120.18	98.97	180	1
cc-pVTZ RCCSD(T)	−168.281 475	3103	1.1454	1.8782	1.0323	120.08	97.51	180	1
cis (C_s)									
DZ(d,p) RHF	−167.664 255	6139	1.1352	1.7576	1.0220	121.18	96.86	0	2
DZ(d,p) CISD[c]	−168.063 587	5464	1.1534	1.8154	1.0376	119.53	95.07	0	2
TZ(2d1f,2p1d) RCCSD	−168.249 046	4843	1.1434	1.8234	1.0367	119.66	94.16	0	2
cc-pVTZ RCCSD(T)	−168.273 508	4852	1.1502	1.8566	1.0369	118.87	93.03	0	2
Fragmentation Products [NH($^3\Sigma^-$)+CO]									
DZ(d,p) RHF	−167.727 206	−7677	1.1174	∞	1.0251				0
DZ(d,p) CISD[c]	−168.102 357	−3045	1.1383	∞	1.0399				0
TZ(2d1f,2p1d) RCCSD	−168.277 072	−1308	1.1252	∞	1.0372				0
cc-pVTZ RCCSD(T)	−168.296 156	−119	1.1325	∞	1.0360				0
Ionization Limit ($\tilde{X}\,^2A''$ HNCO$^+$)									
anti (C_s)[e,f]									
DZ(d,p) RHF	−167.416 203	60 580	1.1024	1.3136	1.0218	173.13	116.45	180	0
PBS EOM-CCSD	−167.884 773	61 331	1.1419	1.2897	1.0410	170.75	118.19	180	0
PBS UCCSD	−167.888 124	62 732	1.1409	1.3023	1.0414	170.80	116.64	180	0
PBS RCCSD	−167.887 410	62 993	1.1379	1.3072	1.0418	170.86	116.09	180	0
TZ(2d1f,2p1d) RCCSD	−167.987 639	62 215	1.1251	1.2875	1.0302	171.20	118.60	180	0
cc-pVTZ RCCSD(T)	−168.013 113	62 001	1.1377	1.2804	1.0289	170.49	119.90	180	

[a] All-electron optimum bond distances in Å and angles in deg. Single-point, frozen-core total energies (E) in hartree, and vibrationless relative energies (ΔE_e) in cm^{-1}. [b] Number of negative-curvature normal modes of full vibrational space. [c] Optimum structure and energy computed with (1s,1s*) core/virtual orbitals frozen. [d] Subject to variational collapse onto lower-energy ^{3}A′ surface. [e] Optimizations of syn starting geometries collapse to anti structures. [f] See ref 137 for 6-311G(*d*,*p*) B3LYP predictions.

equivalent structures on it. The θ[anti → syn] structure **B** is the lowest C_s-symmetry inversion barrier. At the cc-pVTZ RCCSD(T) level (Table 3), when compared to the anti structure, it lies 11 146 cm^{-1} higher in energy, featuring a 0.086 Å N−C bond contraction and an H−N−C framework within 1° of linearity. The alternative ρ[anti → syn] structure **D** occurs at 16 610 cm^{-1}, with N−C and C−O bond lengths similar to **B** but now with an N−C−O angle (176.8°) near linearity. These predictions are in general accord with earlier DZ(d,p)+diffuse CASSCF results.[44] In essence, **B** and **D** are planar inversion barriers accessed, respectively, by steeply descending, complementary H−N−C and N−C−O bending paths emanating from the linear $^3\Delta$(V) stationary point. Whether **B** and **D** on the $\tilde{a}^3A''$ surface are true transition states is dependent on the location of the nearby $\tilde{b}^3A'$ state, as revealed by vertical excitation gaps of the type

$$\Delta E_v(X \rightarrow Y) \equiv E(Y//X) - E(X//X)$$

TABLE 4: Harmonic Vibrational Frequencies (cm^{-1}) of Structures on the $\tilde{a}^3A''$ Surface of Isocyanic Acid

	$\omega_1(a')$ N−H stretch	$\omega_2(a')$ C−O stretch	$\omega_3(a')$ N−C stretch	$\omega_4(a')$ H−N−C bend	$\omega_5(a')$ N−C−O bend	$\omega_6(a'')$ H−N−C−O torsion
Torsional Conformers						
anti (C_s) (**A**)						
DZ(d,p) RHF	3715	2130	1039	1304	635	89
DZ(d,p) CASSCF(8,6)	3722	1851	1062	1293	625	220
DZ(d,p) CISD[a]	3574	1977	935	1235	594	69*i*
TZ(2d1f,2p1d) RCCSD	3458	1856	880	1212	592	168*i*
cc-pVTZ RCCSD(T)	3444	1768	888	1194	585	171*i*
syn (C_s) (**C**)						
DZ(d,p) RHF	3644	2090	1057	1343	586	377*i*
DZ(d,p) CASSCF(8,6)	3654	1870	1059	1335	599	263*i*
DZ(d,p) CISD[a]	3493	1942	953	1284	572	425*i*
cc-pVTZ RCCSD(T)	3328	1735	891	1248	559	536*i*
skewed (trans C_1)						
DZ(d,p) CISD[a]	3572	1971	946	1205	597	94
cc-pVTZ RCCSD(T)[b]	3447	1752	924	1126	586	195
gauche (cis C_1)						
DZ(d,p) RHF	3681	2097	1020	1226	609	271
Inversion Barriers						
ρ [anti → syn] (C_s) (**D**)						
DZ(d,p) RHF	3512	2154	989	1280	1759*i*	444
TZ(2d1f,2p1d) RCCSD	2917	1829	908	1195	1558*i*	378
cc-pVTZ RCCSD(T)	2800	1734	902	1175	1549*i*	380
θ [anti → syn] (C_s) (**B**)						
DZ(d,p) RHF	3988	2033	1208	1200*i*	701	206
TZ(2d1f,2p1d) RCCSD	3736	1621	1063	1133*i*	659	c
cc-pVTZ RCCSD(T)	3737	1471	1052	1102*i*	650	c
Fragmentation Barriers						
trans (C_s)						
DZ(d,p) RHF	3658	2197	1301*i*	1079	477	171
DZ(d,p) CISD[a]	3496	2117	833*i*	979	415	160
TZ(2d1f,2p1d) RCCSD	3363	2086	528*i*	936	402	130
cc-pVTZ RCCSD(T)	3343	2038	481*i*	892	372	150
cis (C_s)						
DZ(d,p) RHF	3593	2162	1617*i*	1102	400	329*i*
DZ(d,p) CISD[a]	3433	2083	1146*i*	1010	343	291*i*
TZ(2d1f,2p1d) RCCSD	3305	2048	644*i*	989	346	292*i*
cc-pVTZ RCCSD(T)	3284	1993	586*i*	949	320	272*i*
Fragmentation Products [NH($^3\Sigma^-$)+CO]						
DZ(d,p) RHF	3552	2424	0	0	0	0
TZ(2d1f,2p1d) RCCSD	3290	2238	0	0	0	0
cc-pVTZ RCCSD(T)	3291	2172	0	0	0	0
Ionization Limit ($\tilde{X}^2A''$ $HNCO^+$)						
anti (C_s)						
DZ(d,p) RHF	3607	2599	1214	939	526	420
TZ(2d1f,2p1d) RCCSD	3419	2203	1169	870	519	488
cc-pVTZ RCCSD(T)	3404	2198	1168	859	484	

[a] Wave function computed with (1s,1s*) core/virtual orbitals frozen. [b] Comparative all-electron cc-pVTZ CCSD(T) harmonic frequencies for ground-state HNCO (at optimum geometry given in footnote a of Table 2): $\omega_1 = 3713$, $\omega_2 = 2330$, $\omega_3 = 1320$, $\omega_4 = 810$, $\omega_5 = 566$, and $\omega_6 = 633$ cm^{-1}. [c] Subject to variational collapse onto lower-energy $^3A'$ surface at this geometry.

where, as usual, // denotes "at the geometry of". Some ΔE_v data are reported in Figure 4 for $(X,Y) = (\tilde{a}^3A'', \tilde{b}^3A')$ at structures **A**−**D** on the $\tilde{a}^3A''$ surface. For **A**, **C**, and **D**, the $\tilde{b}^3A'$ state is located at least 8000 cm^{-1} higher in energy; the cc-pVTZ RCCSD(T) Hessian index of **D** is 1, and the corresponding H−N−C−O torsional frequency is real (380 cm^{-1}, Table 4). However, for **B** the $\tilde{b}^3A'$ state is 4124 cm^{-1} lower in energy, indicating that **B** is not properly an $\tilde{a}$-state transition structure but, owing to a conical intersection, is actually adiabatically connected to the *second* triplet surface of HNCO. While DZ(d,p) RHF theory predicts a real torsional frequency for **B** (206 cm^{-1}), a more reliable result is not accessible to us by coupled-cluster finite-difference methods due to variational collapse obstacles.

To firmly anchor the features of the $\tilde{a}^3A''$ state of HNCO (Tables 3−5, Figures 3 and 4) to the ground electronic state surface, a valence focal-point analysis[40,100,101] was executed for the $\tilde{a}^3A''$ adiabatic excitation energy (T_e). The corresponding layout given in Table 5 pushes the treatment of one-particle basis set and electron correlation effects to technical extremes. The predicted Hartree−Fock limit for T_e is 22 414 cm^{-1}, a value given within 7 cm^{-1} by all basis sets past cc-pVTZ. As expected, the first correlation increment, δ[UMP2], increases the state separation drastically, with a very protracted basis-set dependence. The various extrapolations (n.b., Table 5, footnote *c*) indicate a limiting δ[UMP2] of 12 829 ± 10 cm^{-1}, which is not approached within 100 cm^{-1} even by computations with the prodigious cc-pV6Z basis. Continuing the UMP*n* correlation series for T_e proves to be unproductive, because the successive increments are highly oscillatory and do not appear to have decayed in amplitude below 600 cm^{-1} even at fifth order. The coupled-cluster series is also oscillatory but somewhat better

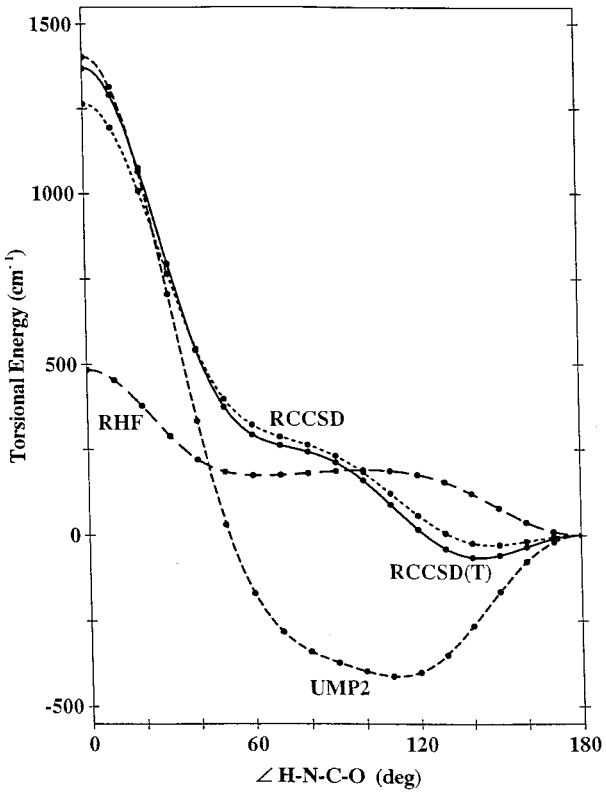

Figure 3. Torsional energy curves for $\tilde{a}^3A''$ HNCO predicted by the cc-pVTZ RHF, UMP2, RCCSD, and RCCSD(T) levels of theory. Data points were generated at 10° intervals along a single path which interpolates the optimum cc-pVTZ RCCSD(T) structures of the anti, skewed, and syn conformers (Table 3), as well as supplementary, constrained ∠(H−N−C−O) = 45° and 90° optimum structures. The form of the fitting functions for geometric variables along the path was $c_0 + c_1 \cos \tau + c_2 \cos 2\tau + c_3 \cos 3\tau + c_4 \cos 4\tau$.

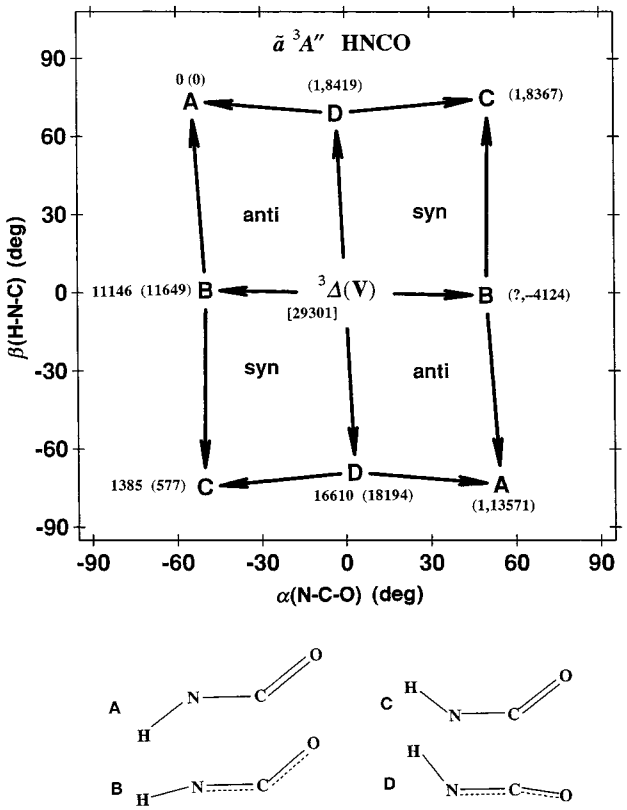

Figure 4. Topology of the potential energy surface for in-plane bending of $\tilde{a}^3A''$ HNCO. α(N−C−O) and β(H−N−C) are linear bending angles measuring distortions from the valence $^3\Delta$ electronic state. Arrows indicate successive downhill paths to four distinct stationary structures, **A**−**D**, as depicted. Toward the left side of the plot appear cc-pVTZ CCSD(T) (DZ(d,p) RHF) sets of energies from Table 3 (ΔE_e, in cm^{-1}) relative to the anti(C_s) structure of the $\tilde{a}^3A''$ state; the corresponding $^3\Delta$(V) energy, shown in brackets, is a PBS EOM-CCSD result. At symmetry-equivalent positions on the right side of the figure, corresponding cc-pVTZ CCSD(T) [Hessian index, $\Delta E_v(\tilde{a}^3A'' \rightarrow \tilde{b}^3A')$] data are given in parentheses.

conditioned. The δ[UCCSD] correction to UMP2 lowers the excitation energy by more than 5000 cm^{-1}, but the ensuing (T) and (Q) shifts are +844 and −329 cm^{-1}, providing a final focal-point (fp) estimate of the valence limit, T_e(fp) = 30 684 cm^{-1}. The core-correlation shift for this excitation energy, as determined at the RCCSD(T) level with the cc-pCVTZ basis,[93] is +192 cm^{-1}. Relativistic effects, gauged by first-order perturbation theory applied to the one-electron mass-velocity and Darwin terms (MVD1),[122] as implemented within the ACESII program suite,[123] result in a correction of −42 cm^{-1} at the cc-pCVTZ RCCSD(T) level. Accounting for these two auxiliary terms leads to a final vibrationless adiabatic excitation energy, T_e(anti) = 30 834 cm^{-1}, for the anti structure on the $\tilde{a}^3A''$ surface. This critical result provides an anchor to the ground state for all of the relative energies (ΔE_e) reported in Tables 1, 3, and 6.

The skewed conformer of triplet HNCO is placed by the best prediction [cc-pVTZ RCCSD(T)] 74 cm^{-1} below the anti form, yielding T_e(skewed) = 30 760 cm^{-1}. The harmonic zero-point vibrational contribution to the excitation energy, as given by the cc-pVTZ RCCSD(T) method, is −671 cm^{-1}, which is revised to −704 cm^{-1} if the large anharmonicity of the torsional vibration of the upper state is considered (vide supra). Therefore, one arrives at the final prediction, T_0 = 30 056 cm^{-1}, for the equilibrium (skewed) structure of lowest triplet state of HNCO.

Very recently Berghout et al.[39] have used a combination of vibrationally mediated photofragment yield spectroscopy and multiphoton fluorescence spectroscopy to determine numerous vibrational term values for the $^1A''$ state of HNCO and hence to locate its band origin, T_0 ($^1A''$) = 32 449 ± 20 cm^{-1}. It is worthwhile to ascertain whether our adiabatic excitation energy determined for the lowest triplet state is in quantitative accord with the empirically derived T_0 for its companion singlet state. The PBS EOM-CCSD method gives an anti minimum for the $^1A''$ state which lies 2905 cm^{-1} above its $\tilde{a}^3A''$ counterpart and exhibits [r_e(C−O), r_e(N−C), r_e(N−H), ρ_e(N−C−O), θ_e(H−N−C)] = (1.2037 Å, 1.3752 Å, 1.0328 Å, 127.00°, 107.40°) and (ω_1, ω_2, ω_3, ω_4, ω_5, ω_6) = (3443, 1720, 1209, 1073, 602, 694) cm^{-1}. Improved, single-point aug-cc-pVTZ[62,124] EOM-CCSD computations at the PBS EOM-CCSD geometries reduce the $^1A''$−$^3A''$ splitting to 2675 cm^{-1}. From T_e(anti $\tilde{a}^3A''$) = 30 834 cm^{-1}, derived above by means of our high-level focal-point analysis with auxiliary corrections, one thus surmises T_e($^1A''$) = 33 509 cm^{-1}, or with the inclusion of PBS EOM-CCSD vibrational shifts, T_0($^1A''$) = 33 196 cm^{-1}. This result is almost 750 cm^{-1} above the empirically derived electronic origin, a difference larger than expected. The source of the discrepancy may lie in the $^1A''$−$^3A''$ splitting, predictions of which have been somewhat erratic.[44] In brief, it is clear that several independent theoretical predictions generally support the recent experimental result for T_0($^1A''$), as summarized in Table 4 of Berghout et al.,[39] but complete certainty via agreement to subchemical accuracy has yet to be achieved.

The dissociation channel $\tilde{a}^3A''$ HNCO → NH($^3\Sigma^-$) + CO is analogous to the extensively investigated[125−135] in-plane bent reaction path for the photofragmentation of triplet ketene into

TABLE 5: Valence Focal-Point Analysis of Critical Energetic Features of the $\tilde{a}^3A''$ HNCO Surface[a,b]

			Series 1					Series 2			
basis set	ΔE_e(UHF)	δ[UMP2]	δ[UMP3]	δ[UMP4]	δ[UMP5]	δ[UMP∞]	ΔE_e(UMP∞)	δ[UCCSD]	δ[UCCSD(T)]	δ[UBD(TQ)]	ΔE_e[UBD(TQ)]
Adiabatic Excitation Energy (T_e): $\tilde{X}^1A' \rightarrow (\tilde{a}^3A''$, anti) HNCO											
cc-pVDZ (47)	**21553**	+11005	−3870	+1601	−2050	+636	**28875**	−4795	+780	−329	**28214**
cc-pVTZ (104)	**22344**	+11936	−4028	+1787	[−2050]	[+636]	**[30625]**	−4983	+839	[−329]	**[29807]**
cc-pVQZ (195)	**22413**	+12452	−4096	+1824	[−2050]	[+636]	**[31179]**	−5074	+844	[−329]	**[30306]**
cc-pV5Z (328)	**22421**	+12632	[−4096]	[+1824]	[−2050]	[+636]	**[31367]**	[−5074]	[+844]	[−329]	**[30494]**
cc-pV6Z (511)	**22416**	+12719	[−4096]	[+1824]	[−2050]	[+636]	**[31449]**	[−5074]	[+844]	[−329]	**[30576]**
extrapolation limit[c] (∞)	**22414**	+12829	[−4096]	[+1824]	[−2050]	[+636]	**[31557]**	[−5074]	[+844]	[−329]	**[30684]**
Fragmentation Barrier (ΔE_e^*): $\tilde{a}^3A''$ HNCO (anti conformer → trans transition state)											
cc-pVDZ (47)	**275**	+2273	−118	−599	+646	−231	**2246**	−493	+49	+39	**2143**
cc-pVTZ (104)	**604**	+2941	−210	−423	[+646]	[−231]	**[3327]**	−617	+124	[+39]	**[3091]**
cc-pVQZ (195)	**694**	+3221	−216	−375	[+646]	[−231]	**[3739]**	−644	+137	[+39]	**[3447]**
cc-pV5Z (328)	**737**	+3313	[−216]	[−375]	[+646]	[−231]	**[3874]**	[−644]	[+137]	[+39]	**[3582]**
cc-pV6Z (511)	**746**	+3356	[−216]	[−375]	[+646]	[−231]	**[3926]**	[−644]	[+137]	[+39]	**[3634]**
extrapolation limit[c] (∞)	**748**	+3413	[−216]	[−375]	[+646]	[−231]	**[3985]**	[−644]	[+137]	[+39]	**[3693]**

[a] The symbol δ denotes the *increment* in the relative energy (ΔE_e) with respect to the preceding level of theory, as given by the competing higher-order correlation series 1 [UHF → UMP2 → UMP3 → UMP4 → UMP5 → UMP∞] and series 2 [UHF → UMP2 → UCCSD → UCCSD(T) → UBD(TQ)]. The higher-order correlation increments listed in brackets are taken for the purpose of extrapolation from corresponding entries for smaller basis sets, thus yielding the net ΔE_e values also appearing in brackets. For each basis set the total number of contracted Gaussian functions is given in parentheses. [b] All total energies were computed at unfrozen-core cc-pVTZ CCSD(T) optimized geometries: ($\tilde{X}\,^1A'$, Table 2, footnote *a*; $\tilde{a}^3A''$, Table 3). In all correlation treatments the 1s core (but no 1s* virtual) orbitals were frozen. [c] UHF and UMP2 basis set extrapolations from $X = (4, 5, 6)$ fits to exponential and X^{-3} forms, respectively. For δ[UMP2] the corresponding $X = (3, 4, 5, 6)$ and $X = (5, 6)$ results for (T_e, ΔE_e^*) are (+12828, +3417) and (+12837, +3416) cm^{-1}, in order.

$^3CH_2$ + CO, which has been a fertile testing ground for both unimolecular reaction theories and innovative high-resolution experiments. The transition state for the HNCO reaction (Table 3) is a trans-planar structure with an N−C distance close to 1.88 Å and a strongly bent H−N−C angle near 98°, connected backward by intrinsic reaction coordinate smoothly to the anti conformer of the $\tilde{a}^3A''$ state, or via late bifurcation of the path to its skewed (C_1) counterpart. At the cc-pVTZ RCCSD(T) level of theory, [r_e(C−O), r_e(N−C), r_e(N−H), ρ_e(N−C−O), θ_e (H−N−C)] change by (−0.045 Å, +0.471 Å, +0.0092 Å, −3.06°, −9.42°) in ascending to the trans fragmentation col from the skewed triplet HNCO minimum. In the critical trans configuration, the elongation of the breaking bond is 33%, and the C−O distance has executed 78% of its contraction toward free carbon monoxide, these percentage variations in the triplet ketene analogue being 51% and 86%, respectively; hence, the isocyanic acid system exhibits an earlier transition state for bond dissociation. Although outward migration of the fragmentation barrier with increasing level of theory is conspicuous in Table 3, this trend is much less pronounced than for triplet ketene, suggesting improved convergence behavior. The harmonic frequencies of the trans fragmentation structure (Table 4) reveal that it is a genuine transition state with a barrier frequency, notably ω_3[cc-pVTZ RCCSD(T)] = 481*i* cm^{-1}, too large to support pronounced step-structure in the dissociation rate constant in the face of tunneling.[134] The data for the cis-planar fragmentation structure in Table 3 reveal that the barrier for internal rotation in the trans col is close to 1770 cm^{-1}, or roughly 400 cm^{-1} *larger* than that for the $\tilde{a}^3A''$ minimum.

At the cc-pVTZ RCCSD(T) level, the trans fragmentation barrier lies 3530 cm^{-1} above the $\tilde{a}^3A''$ anti conformer of HNCO and 4031 cm^{-1} above the NH($^3\Sigma^-$) + CO dissociation products. To refine these energetic predictions, the focal-point analysis detailed in Table 5 was executed. The (anti conformer → trans transition state) barrier (ΔE_e^*) is seen to increase with expansion of the one-particle basis, but somewhat less severely than for T_e. The Hartree−Fock limit for ΔE_e^* is only 748 cm^{-1}, but the estimated MP2 limit is 4161 cm^{-1}, only 59 cm^{-1} removed from the explicit cc-pV6Z MP2 result. The UMP*n* perturbation series for ΔE_e^* is much less oscillatory than for T_e, but the competing coupled-cluster series still displays better convergence properties, the (T) and (Q) corrections being only +137 and +39 cm^{-1}, respectively. Therefore, the best valence focal-point extrapolation yields $\Delta E_e^* = 3693$ cm^{-1}, which is modified to 3767 cm^{-1} upon inclusion of cc-pCVTZ RCCSD(T) core-correlation (+122 cm^{-1}) and relativistic (−48 cm^{-1}) corrections, as computed above. Finally, account must be made for the $\tilde{a}^3A''$ anti → skewed lowering (74 cm^{-1}) and zero-point vibrational effects (−585 cm^{-1}), quantified here by the cc-pVTZ RCCSD(T) harmonic frequencies with amendment as before for the torsional anharmonicity of the skewed structure. We conclude that the ZPVE-corrected transition state for NH($^3\Sigma^-$) + CO dissociation lies 3767 + 74 − 585 = 3256 cm^{-1} above the ground vibrational level on the $\tilde{a}^3A''$ surface. The most recent recommendation[38] for the thermochemical threshold of HNCO($\tilde{X}^1A'$) → NH($^3\Sigma^-$) + CO is $D_0 = 30\,060 \pm 25$ cm^{-1}. In conjunction with our predictions T_0(skewed) = 30 056 cm^{-1} and $\Delta E_e^* = 3256$ cm^{-1}, this bond energy implies that on the $\tilde{a}^3A''$ surface of HNCO, the association barrier for NH($^3\Sigma^-$) + CO is 3252 cm^{-1} and the skewed minimum lies only 4 cm^{-1} below products. This result for the barrier in the ^{3}NH channel (9.3 kcal mol^{-1}) represents a significant upward revision (by 1 to 3 kcal mol^{-1}) of previous B3LYP[41] and CASPT2[44] predictions, and its magnitude is about seven times larger than the barrier in the ^{1}NH channel.[38]

V. The $\tilde{b}^3A'$ Surface

An exploration of the potential energy surface of the valence $\tilde{b}^3A'$ state of HNCO is recorded in Tables 6 and 7, where stationary structures and harmonic vibrational frequencies for several in-plane minima and interconversion barriers are reported, along with comparative results for the appropriate excited-state ionization limit ($^2\Pi$ $HNCO^+$). Again, greatest attention should be focused on the complete set of data given by the high-level cc-pVTZ RCCSD(T) method. Figure 5 is a map that elucidates the intricate interconnections and relative energies of the various structures occurring within the planar configuration space of the second triplet state of HNCO.

TABLE 6: Stationary Points on the $\tilde{b}^3A'$ Surface of Isocyanic Acid[a]

	E	ΔE_e[b]	ΔE_v[c]	r_e(C−O)	r_e(N−C)	r_e(N−H)	ρ_e(N−C−O)	θ_e(H−N−C)	τ_e(H−N−C−O)	Hessian index[d]
In-Plane Minima										
anti (N═C−O) (**A**)										
DZ(d,p) RHF	−167.662 926	6430	−209	1.3478	1.2188	1.0009	122.08	121.22	180	0
DZ(d,p) CASSCF(8,6)	−167.711 175	6678	−	1.311	1.248	0.998	118.7	128.4	180	0
DZ(d,p) CISD[e]	−168.056 896	6933	1882	1.3090	1.2486	1.0058	117.09	132.43	180	1
TZ(2d1f,2p1d) RCCSD	−168.243 965	5958	1534	1.2613	1.2583	1.0002	117.69	139.36	180	
cc-pVTZ RCCSD(T)	−168.268 594	5930	1035	1.2666	1.2610	0.9993	117.92	139.30	180	1
syn (N═C−O) (**E**)										
DZ(d,p) RHF	−167.656 677	7802	−300	1.3479	1.2131	1.0058	128.19	122.80	0	0
syn (N−C═O) (**C**)										
DZ(d,p) RHF	−167.671 134	4629	1398	1.1769	1.3313	1.0021	127.41	138.44	0	1
DZ(d,p) CASSCF(8,6)	−167.717 631	5261	−	1.205	1.309	1.001	124.8	138.5	0	1
DZ(d,p) CISD[e]	−168.066 973	4721	3059	1.2115	1.3137	1.0123	124.33	139.28	0	1
TZ(2d1f,2p1d) RCCSD	−168.253 233	3924	3068	1.2111	1.2922	1.0106	124.62	137.87	0	
cc-pVTZ RCCSD(T)	−168.278 618	3730	3320	1.2251	1.2879	1.0104	124.51	137.64	0	1
In-Plane Barriers										
anti (N═C−O) → syn (N−C═O) (**B**)										
DZ(d,p) RHF	−167.654 596	8259	3104	1.1816	1.3236	0.9902	123.56	165.78	180	2
DZ(d,p) CISD[e]	−168.054 152	7535	4380	1.2142	1.3109	0.9988	121.10	164.86	180	2
TZ(2d1f,2p1d) RCCSD	−168.241 066	6594	5672	1.2328	1.2749	0.9941	119.88	170.07	180	
cc-pVTZ RCCSD(T)	−168.265 732	6558	5168	1.2387	1.2766	0.9930	120.01	168.42	180	2
syn (N−C═O) → syn (N═C−O) (**D**)										
DZ(d,p) RHF	−167.655 275	8110	1736	1.3022	1.2139	0.9999	125.55	136.78	0	2
syn (N═C−O) → anti (N═C−O) (**F**)										
DZ(d,p) RHF	−167.581 950	24203	5362	1.3409	1.2243	1.0191	176.99	119.19	180	1
syn (N−C═O) → anti (N═C−O) (**F**)										
TZ(2d1f,2p1d) RCCSD	−168.171 167	21935	−1934	1.2457	1.2538	1.0444	174.42	130.91	180	
cc-pVTZ RCCSD(T)	−168.197 412	21553	−2158	1.2464	1.2626	1.0469	174.13	130.58	180	f
Ionization Limit ($^2\Pi$ $HNCO^+$)										
DZ(d,p) RHF	−167.398 496	64466		1.1142	1.2340	1.0128	180	180		2
PBS RCCSD	−167.871 948	66387		1.1654	1.2180	1.0264	180	180		
TZ(2d1f,2p1d) RCCSD	−167.975 609	64856		1.1522	1.2041	1.0159	180	180		
cc-pVTZ RCCSD(T)	−168.002 034	64433		1.1676	1.2009	1.0145	180	180		1

[a] All-electron optimum bond distances in Å and angles in deg; single-point, frozen-core total energies (E) in hartree, and vibrationless relative energies (ΔE_e, ΔE_v) in cm^{-1}. [b] Energy of the $\tilde{b}^3A'$ state relative to the anti(C_s) structure of the $\tilde{a}^3A''$ state. [c] $\Delta E_v(\tilde{b}^3A' \rightarrow \tilde{a}^3A'')$, as defined in text. [d] Number of negative-curvature normal modes of full vibrational space. [e] Wave function computed with (1s,1s*) core/virtual orbitals frozen. [f] Subject to variational collapse onto lower-energy $^3A''$ surface.

Molecular bending from the $^3\Sigma^+$(V) linear structure (Table 1 and Figure 2) yields $\tilde{b}^3A'$ HNCO, which upon complete in-plane optimization drops in energy on the order of 20 000 cm^{-1}, or about two-thirds of the analogous $^3\Delta$(V) stabilization on the $\tilde{a}^3A''$ surface. The $\tilde{b}^3A'$ state becomes ($9a' \rightarrow 10a'$) in electronic character and adopts two competing geometric forms at all levels of theory. The first structure is anti (N═C−O) (**A**), which cc-pVTZ RCCSD(T) theory locates 5930 cm^{-1} above the anti $\tilde{a}^3A''$ reference point. The cc-pVTZ RCCSD(T) geometry of **A** for the $\tilde{b}^3A'$ state displays C−O and N−C distances elongated by 0.100 Å and 0.045 Å, respectively, vis-à-vis the ground state (footnote *a* of Table 2), and thus, unlike the **A** structure of the $\tilde{a}^3A''$ state, the electronic excitation has primarily weakened the C−O rather than the N−C bond. Moreover, at the same level of theory, $\tilde{b}^3A'$ structure **A** has an N−C−O angle decreased by 7.4° and an H−N−C framework widened by 32.8° with respect to its $\tilde{a}^3A''$ counterpart. In Table 6 it is seen that the RHF, CASSCF(8,6), and CISD methods exaggerate the C−O elongation and underestimate the H−N−C widening in $\tilde{b}^3A'$ structure **A**.

The second, and lowest-energy, structure on the $\tilde{b}^3A'$ surface is syn (N−C═O) (**C**). At the cc-pVTZ RCCSD(T) level, this structure lies only 3730 cm^{-1} above anti $\tilde{a}^3A''$ (**A**), while r_e(C−O) and r_e(N−C) are 0.058 Å and 0.071 Å longer, respectively, than in the ground state. Thus, $\tilde{b}^3A'$ structure **C** basically has formal N−C═O character, similar to **C** on the $\tilde{a}^3A''$ surface, although in the former case the N−C distance is over 0.1 Å shorter and the H−N−C angle is over 30° larger.

The DZ(d,p) RHF surface for $\tilde{b}^3A'$ HNCO exhibits spurious features arising from the ease of heavy-atom bond fluctuations and large-amplitude H−N−C bending. In addition to **A** and **C**, there exists a formal syn (N═C−O) structure (**E**), whose bond distances and angles closely mirror those of its anti (N═C−O) counterpart. At the DZ(d,p) RHF level, **E** appears 3173 cm^{-1} above **C**, to which it is connected via transition structure **D**, constituting an **E** → **C** barrier of only 308 cm^{-1}. At correlated levels of theory, this barrier disappears, and **E** collapses into **C**.

The harmonic vibrational frequencies in Table 7 provide final characterization of the stationary structures on the $\tilde{b}^3A'$ surface. Whereas all of the in-plane minima are positive definite in the C_s configuration space, negative curvature for torsional distortions is responsible for an overall Hessian index of 1 in many cases. At all levels of theory, the curvature for the torsional mode is a direct consequence of the vertical state separations $\Delta E_v(\tilde{b}^3A' \rightarrow \tilde{a}^3A'')$ listed in Table 6. When $\Delta E_v < 0$, the $^3A'$ state lies above the $^3A''$ state, is repelled by the lower state upon out-of-plane distortions, and exhibits positive torsional curvature. When $\Delta E_v > 0$, the $^3A'$ state lies below the $^3A''$ state due to some nearby conical intersection, is connected smoothly to structures a few thousand cm^{-1} lower in energy on the $\tilde{a}^3A''$ surface via meandering excursions into the full geometric configuration space, and displays negative torsional curvature. Accordingly, in Table 6 the RHF and CASSCF(8,6) structures for **A** and/or **E** have a Hessian index of 0, whereas for **C** this index is 1, even though it lies significantly lower in energy. In

TABLE 7: Harmonic Vibrational Frequencies (cm^{-1}) of Structures on the $\tilde{b}^3A'$ Surface of Isocyanic Acid

	$\omega_1(a')$ N−H stretch	$\omega_2(a')$ C−O stretch	$\omega_3(a')$ N−C stretch	$\omega_4(a')$ H−N−C bend	$\omega_5(a')$ N−C−O bend	$\omega_6(a'')$ H−N−C−O torsion
			In-Plane Minima			
anti (N═C−O) (**A**)						
DZ(d,p) RHF	3857	1220	1967	958	523	2394
DZ(d,p) CASSCF(8,6)	3890	1124	1690	899	477	1598
DZ(d,p) CISD[a]	3822	1264	2607[b]	971	646	1180*i*
cc-pVTZ RCCSD(T)	3745	1513	718	1170	540	1954*i*
syn (N═C−O) (**E**)						
DZ(d,p) RHF	3777	1234	2020	720	538	1850
syn (N−C═O) (**C**)						
DZ(d,p) RHF	3829	1999	1362	1059	572	1755*i*
DZ(d,p) CASSCF(8,6)	3850	1357	1678	1025	562	1685*i*
DZ(d,p) CISD[a]	3712	1631	1320	960	523	1184*i*
cc-pVTZ RCCSD(T)	3567	1485	1382	928	536	1034*i*
			In-Plane Barriers			
anti (N═C−O) → syn (N−C═O) (**B**)						
DZ(d,p) RHF	4013	1793	1313	693*i*	539	1117*i*
DZ(d,p) CISD[a]	3928	2426[b]	1477	532*i*	723	1034*i*
cc-pVTZ RCCSD(T)	3849	1231	1433	682*i*	578	828*i*
syn (N−C═O) → syn (N═C−O) (**D**)						
DZ(d,p) RHF	3860	1527*i*	1721	1110	555	740*i*
syn (N═C−O) → anti (N═C−O) (**F**)						
DZ(d,p) RHF	3465	2104	1097	882	1465*i*	477
syn (N→ anti (N═C−O) (**F**)						
cc-pVTZ RCCSD(T)	2609	1894[c]	1086[c]	1074[c]	1294*i*	*d*
			Ionization Limit ($^2\Pi$ $HNCO^+$)[e]			
DZ(d,p) RHF	3722	2576	1414	$\omega_{4a,4b}(\pi) = 712i$, 178*i* HNC bend $\omega_{5a,5b}(\pi) = 644$, 578 NCO bend		
cc-pVTZ RCCSD(T)	3589	1786	1337	$\omega_{4a,4b}(\pi) = 517i$, 469 HNC bend $\omega_{5a,5b}(\pi) = 562$, 526 NCO bend		

[a] Wave function computed with (1s,1s*) core/virtual orbitals frozen. [b] Anomalous predictions given by DZ(d,p) CISD theory. [c] Strongly mixed normal modes. [d] Subject to variational collapse onto lower-energy $^3A''$ surface. [e] Degenerate bending frequencies are split due to Renner−Teller effect.

the dynamically correlated treatments, both **A** and **C** have negative torsional curvature due to inversion of state ordering. At the highest level of theory [cc-pVTZ RCCSD(T)], it is thus concluded that *there are no legitimate, stable minima on the* $\tilde{b}^3A'$ *surface of isocyanic acid*, only planar stationary points (in-plane minima) connected via torsional transformations to the lowest triplet surface as a consequence of conical intersections. Strictly speaking, the lowest-energy structures on the genuinely adiabatic, second triplet surface of HNCO occur in the wells of conical intersections, a phenomenon which also occurs for the isoelectronic ketene molecule.[136]

The in-plane barriers in Table 6 mediate interconversions in C_s configuration space among in-plane minima on the $\tilde{b}^3A'$ surface. The schematic two-dimensional linear bending surface in Figure 5 reveals that H−N−C inversion is the preferred route between structures **A** and **C**. In the attendant transition structure **B**, at the cc-pVTZ RCCSD(T) level, the H−N−C angle is 168° in a trans orientation, the coordinates of the N−C−O framework nicely interpolate those of **A** and **C**, and the **A** → **C** barrier is merely 628 cm^{-1}. Earlier DZ(d,p)+diffuse CASSCF results[44] give a similar barrier, but **A** and **C** are reported to be genuine minima, and whereas their preferred interconversion path also involves H−N−C inversion, the structure analogous to **B** has a C−O distance (1.156 Å) that is anomalously small. The alternative inversion path between **A** and **C** is highly hindered, with transition structure **F** in our work having an N−C−O angle within 6° of linearity, lying over 15 000 cm^{-1} above **A**. The cc-pVTZ RCCSD(T) method predicts a trans orientation in **F**, with heavy-atom distances between those of **A** and **C**, but (in contrast) an unusually elongated N−H bond length (1.047 Å) and an H−N−C angle bent down to 130.6°. At structure **B**, the $^3A'$ state lies over 5000 cm^{-1} below its $^3A''$ companion, engendering negative torsional curvature and an overall Hessian index of 2 (see Table 7). At **F**, the normal state ordering is preserved, the $^3A'$ state lying higher by about 2000 cm^{-1}.

Conclusions

Winnowing the triplet electronic states of HNCO up to 80 000 cm^{-1} in excitation energy reveals that the lowest states correlate to a [$^3\Sigma^+$(V), $^3\Delta$(V), $^3\Pi$(R), $^3\Sigma^-$(V)] manifold at linear geometries lying in the 54 000 to 64 000 cm^{-1} range. The valence states in this regime all arise from $2\pi \rightarrow 3\pi$ excitations, and the $^3\Pi$ Rydberg state, which fragments monotonically to $H(^2S) + NCO(\tilde{X}\ ^2\Pi)$, is of $2\pi \rightarrow 3s$ character. The valence states are substantially lowered in energy by bending of the molecular framework, bringing them into the range of the numerous photolysis experiments that have probed HNCO dissociation over the last 15 years. The bending potential curves of triplet HNCO electronic states exhibit numerous actual intersections and avoided crossings, the most significant being the valence−valence $\tilde{a}^3A''/\tilde{b}^3A'$ intersection and the valence−Rydberg $\tilde{a}^3A''/\tilde{c}^3A''$ avoided crossing near H−N−C angles of 136° and 150°, respectively. The diabatic connections, which can be followed through these crossings, show that the [$^3\Sigma^+$(V), $^3\Delta$(V), $^3\Pi$(R), $^3\Sigma^-$(V)] cluster gives rise to the [$\tilde{b}^3A'$, ($\tilde{d}\ ^3A'$,$\tilde{a}^3A''$), ($\tilde{e}^3A'$,$\tilde{c}^3A''$), $\tilde{f}\ ^3A''$] states.

The $\tilde{a}^3A''$ state, of ($2a'' \rightarrow 10a'$) character, settles into equivalent skewed (trans-C_1) minima with r_e(C−O) = 1.19 Å, r_e(N−C) = 1.41 Å, r_e(N−H) = 1.02 Å, ρ_e(N−C−O) = 123°, θ_e(H−N−C) = 107°, τ_e(H−N−C−O) = ±143°, and a predicted adiabatic excitation energy T_0 = 30 056 cm^{-1}. The barrier

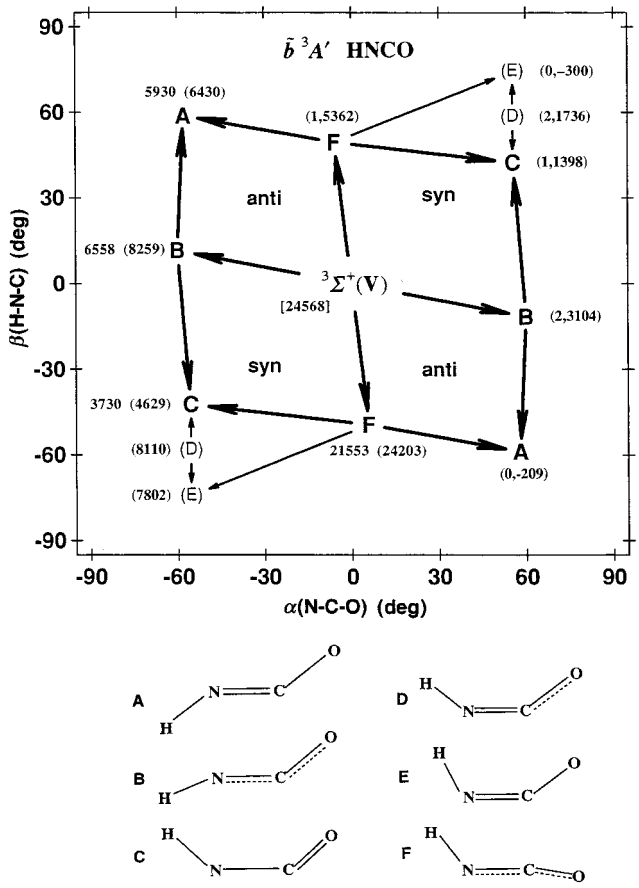

Figure 5. Topology of the potential energy surface for in-plane bending of $\tilde{b}^3A'$ HNCO (*à la* Figure 4), starting from the valence $^3\Sigma^+$ electronic state. Structures **D** and **E**, which are shown in parentheses and exist only at the DZ(d,p) RHF level, are separated from **C** mostly by antisymmetric (C−O, N−C) stretching rather than bending displacements, and thus their positions in the figure are distorted for the sake of clarity. Moreover, at the symmetry-equivalent positions on the right side of the figure, DZ(d,p) RHF [Hessian index, $\Delta E_v(\tilde{b}^3A' \rightarrow \tilde{a}^3A'')$] entries from Table 5 are displayed in parentheses, revealing locations of $\tilde{a}^3A''/\tilde{b}^3A'$ conical intersections before inclusion of electron correlation effects. For the $\tilde{b}^3A'$ stationary points given by the cc-pVTZ CCSD(T) method, the $\tilde{b}^3A'$ state lies *below* its $\tilde{a}^3A''$ counterpart at **A**, **B**, and **C**, but above at **F**.

to trans-planarity of these minima is a mere 74 cm^{-1}, and the ground vibrational state appears to lie less than 10 cm^{-1} below this barrier (the anti structure). The ascent on the $\tilde{a}^3A''$ torsional potential out of the skewed minima and away from trans configurations passes through gauche shoulders before arriving at a syn (or cis) maximum about 1460 cm^{-1} higher in energy. In-plane anti/syn interconversions can occur on the $\tilde{a}^3A''$ surface via a preferred H−N−C bending route with just over 11 000 cm^{-1} of vibrational energy. Remarkably, the skewed $\tilde{a}^3A''$ minima are predicted to be almost perfectly isoenergetic with the dissociation products of channel (1), $NH(X^3\Sigma^-)$ + $CO(X^1\Sigma^+)$, the intervening trans fragmentation col occurring at an N−C distance of 1.88 Å and exhibiting a zero-point corrected barrier of 3256 cm^{-1}.

The ($9a' \rightarrow 10a'$) $\tilde{b}^3A'$ state of HNCO is found to be highly fluxional, possessing both facile bond fluctuations in the NCO moiety and large-amplitude H−N−C bending. In C_s configuration space, it achieves its lowest energy in a syn(N−C═O) structure with r_e(C−O) = 1.23 Å, r_e(N−C) = 1.29 Å, r_e(N−H) = 1.01 Å, ρ_e(N−C−O) = 125°, and θ_e(H−N−C) = 138°, appearing only about 3800 cm^{-1} above the $\tilde{a}^3A''$ minima, which makes the $\tilde{b}^3A'$ surface accessible from S_0 with 34 000 cm^{-1} photons. In-plane anti/syn interconversions on the $\tilde{b}^3A'$ surface once again prefer an H−N−C bending route, but in this case less than 3000 cm^{-1} of vibrational energy is required. More importantly, the $\tilde{b}^3A'$ planar, minimum-energy syn(N−C═O) structure proves to have negative curvature for torsional distortions as a consequence of a conical intersection with the $\tilde{a}^3A''$ state. Accordingly, the $\tilde{b}^3A'$ surface has no legitimate, stable minima, only planar stationary points connected via torsional transformations to the lowest triplet surface. In other words, the lowest-energy structures on the genuinely adiabatic, second triplet surface of HNCO occur in the wells of conical intersections. The key conclusion regarding the photodissociation dynamics of HNCO is that the $\tilde{a}^3A''$ and $\tilde{b}^3A'$ surfaces are firmly interlocked, even at low energies. While a narrow window of about 500 cm^{-1} exists above the threshold to channel (1) where only the $\tilde{a}^3A''$ surface is accessed, by the time channel (2) opens there is virtually a complete interweaving of both HNCO surfaces. This phenomenon clearly augments the richness of isocyanic acid fragmentation dynamics.

Acknowledgment. The research at the Center for Computational Quantum Chemistry at the University of Georgia was supported by the U.S. Department of Energy, Office of Basic Energy Sciences, Fundamental Interactions Branch, Grant No. DE-FG02-00ER14748. The work of A.G.C. was also supported by the Hungarian Ministry of Culture and Education (FKFP 0117/1997) and by the Scientific Research Foundation of Hungary (OTKA T024044). International exchanges between Georgia and Hungary were supported by a NATO Linkage Grant (CRG.LG 973 892).

References and Notes

(1) Teles, J. H.; Maier, G.; Hess, B. A., Jr.; Schaad, L. J.; Winnewisser, M.; Winnewisser, B. P. *Chem. Ber.* **1989**, *122*, 753.
(2) Winnewisser, B. P. In *Molecular Spectroscopy: Modern Research*; K. N. Rao, Ed.; Academic Press: New York, 1985; Vol. III.
(3) East, A. L. L.; Johnson, C. S.; Allen, W. D. *J. Chem. Phys.* **1993**, *98*, 1299.
(4) Dixon, R. N.; Kirby, G. H. *Trans. Faraday Soc.* **1968**, *64*, 2002.
(5) Rabalais, J. W.; McDonald, J. R.; McGlynn, S. P. *J. Chem. Phys.* **1969**, *51*, 5103.
(6) Okabe, H. *J. Chem. Phys.* **1970**, *53*, 3507.
(7) Spiglanin, T. A.; Perry, R. A.; Chandler, D. W. *J. Phys. Chem.* **1986**, *90*, 6184.
(8) Spiglanin, T. A.; Perry, R. A.; Chandler, D. W. *J. Chem. Phys.* **1987**, *87*, 1568.
(9) Spiglanin, T. A.; Chandler, D. W. *J. Chem. Phys.* **1987**, *87*, 1577.
(10) Spiglanin, T. A.; Chandler, D. W. *Chem. Phys. Lett.* **1987**, *141*, 428.
(11) Hikida, T.; Maruyama, Y.; Saito, Y.; Mori, Y. *Chem. Phys.* **1988**, *121*, 63.
(12) Quiñones, E.; Chen, J.; Dagdigian, P. J. *Chem. Phys. Lett.* **1990**, *174*, 65.
(13) Uno, K.; Hikida, T.; Hiraya, A.; Shobatake, K. *Chem. Phys. Lett.* **1990**, *166*, 475.
(14) Yi, W.; Bersohn, R. *Chem. Phys. Lett.* **1993**, *206*, 365.
(15) Bohn, B.; Stuhl, F. *J. Phys. Chem.* **1993**, *97*, 4891.
(16) Ruscic, B.; Berkowitz, J. *J. Chem. Phys.* **1994**, *100*, 4498.
(17) Brown, S. S.; Berghout, H. L.; Crim, F. F. *J. Chem. Phys.* **1995**, *102*, 8440.
(18) Zhang, J.; Dulligan, M.; Wittig, C. *J. Phys. Chem.* **1995**, *99*, 7446.
(19) Brown, S. S.; Berghout, H. L.; Crim, F. F. *J. Phys. Chem.* **1996**, *100*, 7948.
(20) Brown, S. S.; Metz, R. B.; Berghout, H. L.; Crim, F. F. *J. Chem. Phys.* **1996**, *105*, 6293.
(21) Brown, S. S.; Berghout, H. L.; Crim, F. F. *J. Chem. Phys.* **1996**, *105*, 8103.
(22) Brown, S. S.; Cheatum, C. M.; Fitzwater, D. A.; Crim, F. F. *J. Chem. Phys.* **1996**, *105*, 10911.
(23) Zyrianov, M.; Droz-Georget, T.; Sanov, A.; Reisler, H. *J. Chem. Phys.* **1996**, *105*, 8111.
(24) Brownsword, R. A.; Laurent, T.; Vatsa, R. K.; Volpp, H.-R.; Wolfrum, J. *Chem. Phys. Lett.* **1996**, *258*, 164.

(25) Brownsword, R. A.; Laurent, T.; Vatsa, R. K.; Volpp, H.-R.; Wolfrum, J. *Chem. Phys. Lett.* **1996**, *249*, 162.
(26) Kawasaki, M.; Sato, Y.; Suto, K.; Matsumi, Y.; Wilson, S. H. S. *Chem. Phys. Lett.* **1996**, *251*, 67.
(27) Brown, S. S.; Berghout, H. L.; Crim, F. F. *J. Chem. Phys.* **1997**, *106*, 5805.
(28) Brown, S. S.; Berghout, H. L.; Crim, F. F. *J. Chem. Phys.* **1997**, *107*, 8985.
(29) Brown, S. S.; Berghout, H. L.; Crim, F. F. *J. Chem. Phys.* **1997**, *107*, 9764.
(30) Droz-Georget, T.; Zyrianov, M.; Reisler, H.; Chandler, D. W. *Chem. Phys. Lett.* **1997**, *276*, 316.
(31) Sanov, A.; Droz-Georget, T.; Zyrianov, M.; Reisler, H. *J. Chem. Phys.* **1997**, *106*, 7013.
(32) Zyrianov, M.; Droz-Georget, T.; Reisler, H. *J. Chem. Phys.* **1997**, *106*, 7454.
(33) Droz-Georget, T.; Zyrianov, M.; Sanov, A.; Reisler, H. *Ber. Bunsen-Ges. Phys. Chem.* **1997**, *101*, 469.
(34) Brownsword, R. A.; Hillenkamp, M.; Laurent, T.; Vatsa, R. K.; Volpp, H.-R. *J. Chem. Phys.* **1997**, *106*, 4436.
(35) Brownsword, R. A.; Laurent, T.; Hillenkamp, M.; Vatsa, R. K.; Volpp, H.-R. *J. Chem. Phys.* **1997**, *106*, 9563.
(36) Berghout, H. L.; Brown, S. S.; Delgado, R.; Crim, F. F. *J. Chem. Phys.* **1998**, *109*, 2257.
(37) Coffey, M. J.; Berghout, H. L.; Woods, E., III; Crim, F. F. *J. Chem. Phys.* **1999**, *110*, 10850.
(38) Zyrianov, M.; Droz-Georget, T.; Reisler, H. *J. Chem. Phys.* **1999**, *110*, 2059.
(39) Berghout, H. L.; Crim, F. F.; Zyrianov, M.; Reisler, H. *J. Chem. Phys.* **2000**, *112*, 6678.
(40) East, A. L. L.; Allen, W. D. *J. Chem. Phys.* **1993**, *99*, 4638.
(41) Mebel, A. M.; Luna, A.; Lin, M. C.; Morokuma, K. *J. Chem. Phys.* **1996**, *105*, 6439.
(42) Fang, W.-H.; You, X.-Z.; Yin, Z. *Chem. Phys. Lett.* **1995**, *238*, 236.
(43) Stevens, J. E.; Cui, Q.; Morokuma, K. *J. Chem. Phys.* **1998**, *108*, 1452.
(44) Kaledin, A. L.; Cui, Q.; Heaven, M. C.; Morokuma, K. *J. Chem. Phys.* **1999**, *111*, 5004.
(45) Klossika, J.-J.; Flöthmann, H.; Beck, C.; Schinke, R.; Yamashita, K. *Chem. Phys. Lett.* **1997**, *276*, 325.
(46) Klossika, J.-J.; Schinke, R. *J. Chem. Phys.* **1999**, *111*, 5882.
(47) Klossika, J.-J.; Flöthmann, H.; Schinke, R.; Bittererová, M. *Chem. Phys. Lett.* **1999**, *314*, 182.
(48) Mertens, J. D.; Chang, A. Y.; Hanson, R. K.; Bowman, C. T. *Int. J. Chem. Kinet.* **1989**, *21*, 1049.
(49) Perry, R. A.; Siebers, D. L. *Nature* **1986**, *324*, 657.
(50) Miller, J. A.; Bowman, C. T. *Prog. Energy Comb. Sci.* **1989**, *15*, 287.
(51) Lin, M. C.; He, Y.; Melius, C. F. *Int. J. Chem. Kinet.* **1992**, *24*, 1103.
(52) He, Y.; Liu, X.; Lin, M. C.; Melius, C. F. *Int. J. Chem. Kinet.* **1991**, *23*, 1129.
(53) Zhao, X.; Hinsta, E. J.; Lee, Y. T. *J. Chem. Phys.* **1988**, *88*, 801.
(54) Huzinaga, S. *J. Chem. Phys.* **1965**, *42*, 1293.
(55) Dunning, T. H., Jr. *J. Chem. Phys.* **1970**, *53*, 2823.
(56) Dunning, T. H., Jr. *J. Chem. Phys.* **1971**, *55*, 716.
(57) Dunning, T. H., Jr. *J. Chem. Phys.* **1989**, *90*, 1007.
(58) Sadlej, A. J. *Collect. Czech. Chem. Commun., Part I* **1988**, *53*, 1995.
(59) Sadlej, A. J. *Theor. Chim. Acta* **1991**, *79*, 123.
(60) Szalay, P. G.; Császár, A. G.; Nemes, L. *J. Chem. Phys.* **1996**, *105*, 1034.
(61) Wilson, A. K.; van Mourik, T.; Dunning, T. H., Jr. *J. Mol. Struct. (THEOCHEM)* **1996**, *388*, 339.
(62) Extensible Computational Chemistry Environment Basis Set Database, Version 1.0, as developed and distributed by the Molecular Science Computing Facility, Environmental and Molecular Sciences Laboratory, which is part of the Pacific Northwest Laboratory, P.O. Box 999, Richland, WA 99352, USA and funded by the U.S. Department of Energy. The Pacific Northwest Laboratory is a multi-program laboratory operated by Battelle Memorial Institute for the U.S. Department of Energy under contract DE-AC06−76RLO 1830.
(63) Roothaan, C. C. J. *Rev. Mod. Phys.* **1951**, *23*, 69.
(64) Hehre, W. J.; Radom, L.; Schleyer, P. v. R.; Pople, J. A. *Ab Initio Molecular Orbital Theory*; Wiley-Interscience: New York, 1986.
(65) Pople, J. A.; Nesbet, R. K. *J. Chem. Phys.* **1954**, *22*, 571.
(66) Szabo, A.; Ostlund, N. S. *Modern Quantum Chemistry: Introduction to Advanced Electronic Structure Theory*, 1st ed., revised; McGraw-Hill: New York, 1989.
(67) Roos, B. O. In *Ab Initio Methods in Quantum Chemistry, Part II*; K. P. Lawley, Ed.; Wiley & Sons: New York, 1987; pp 399−445.
(68) Shavitt, I. In *Modern Theoretical Chemistry*; Schaefer, H. F., III, Ed.; Plenum: New York, 1977; Vol. 3; pp 189−275.
(69) Brooks, B. R.; Schaefer, H. F., III *J. Chem. Phys.* **1979**, *70*, 5092.
(70) Saxe, P.; Fox, D. J.; Schaefer, H. F., III; Handy, N. C. *J. Chem. Phys.* **1982**, *77*, 5584.
(71) Pople, J. A.; Binkley, J. S.; Seeger, R. *Int. J. Quantum Chem. Symp.* **1976**, *10*, 1.
(72) Krishnan, R.; Pople, J. A. *Int. J. Quantum Chem.* **1978**, *14*, 91.
(73) Krishnan, R.; Frisch, M. J.; Pople, J. A. *J. Chem. Phys.* **1980**, *72*, 4244.
(74) Raghavachari, K.; Pople, J. A.; Replogle, E. S.; Head-Gordon, M. *J. Phys. Chem.* **1990**, *94*, 5579.
(75) Bartlett, R. J. *Annu. Rev. Phys. Chem.* **1981**, *32*, 359.
(76) Purvis, G. D.; Bartlett, R. J. *J. Chem. Phys.* **1982**, *76*, 1910.
(77) Paldus, J. In *New Horizons of Quantum Chemistry*; Löwdin, P.-O., Pullmann, B., Eds.; Reidel: Dordrecht, 1983; pp 31−60.
(78) Bartlett, R. J.; Dykstra, C. E.; Paldus, J. In *Advanced Theories and Computational Approaches to the Electronic Structure of Molecules*; Dykstra, C. E., Ed.; Reidel: Dordrecht, 1984; pp 127−159.
(79) Scuseria, G. E.; Scheiner, A. C.; Lee, T. J.; Rice, J. E.; Schaefer, H. F., III *J. Chem. Phys.* **1987**, *86*, 2881.
(80) Raghavachari, K.; Trucks, G. W.; Pople, J. A.; Head-Gordon, M. *Chem. Phys. Lett.* **1989**, *157*, 479.
(81) Scuseria, G. E.; Lee, T. J. *J. Chem. Phys.* **1990**, *93*, 5851.
(82) Handy, N. C.; Pople, J. A.; Head-Gordon, M.; Raghavachari, K.; Trucks, G. W. *Chem. Phys. Lett.* **1989**, *164*, 185.
(83) Lee, T. J.; Kobayashi, R.; Handy, N. C.; Amos, R. D. *J. Chem. Phys.* **1992**, *96*, 8931.
(84) Rittby, M.; Bartlett, R. J. *J. Phys. Chem.* **1988**, *92*, 3033.
(85) Gauss, J.; Lauderdale, W. J.; Stanton, J. F.; Watts, J. D.; Bartlett, R. J. *Chem. Phys. Lett.* **1991**, *182*, 207.
(86) Watts, J. D.; Gauss, J.; Bartlett, R. J. *J. Chem. Phys.* **1993**, *98*, 8718.
(87) Crawford, T. D.; Schaefer, H. F., III *J. Chem. Phys.* **1996**, *104*, 6259.
(88) Stanton, J. F.; Bartlett, R. J. *J. Chem. Phys.* **1993**, *98*, 7029.
(89) Meissner, L.; Bartlett, R. J. *J. Chem. Phys.* **1991**, *94*, 6670.
(90) Nooijen, M.; Snijders, J. G. *Int. J. Quantum Chem.* **1993**, *48*, 15.
(91) Nooijen, M.; Snijders, J. G. *J. Chem. Phys.* **1995**, *102*, 1681.
(92) Stanton, J. F.; Gauss, J. *J. Chem. Phys.* **1994**, *101*, 8938.
(93) Woon, D. E.; Dunning, T. H., Jr. *J. Chem. Phys.* **1995**, *103*, 4572.
(94) Yamaguchi, Y.; Osamura, Y.; Goddard, J. D.; Schaefer, H. F., III *A New Dimension to Quantum Chemistry: Analytic Derivative Methods in Ab Initio Molecular Electronic Structure Theory*; Oxford University Press: New York, 1994.
(95) Stanton, J. F. *J. Chem. Phys.* **1993**, *99*, 8840.
(96) Stanton, J. F.; Gauss, J. *J. Chem. Phys.* **1994**, *100*, 4695.
(97) Lauderdale, W. J.; Cheng, V. G.; Wierschke, S. G. *J. Phys. Chem.* **1994**, *98*, 4502.
(98) Jayatilaka, D.; Lee, T. J. *J. Chem. Phys.* **1993**, *98*, 9734.
(99) Lee, T. J.; Taylor, P. R. *Int. J. Quantum Chem. Symp.* **1989**, *23*, 199.
(100) Császár, A. G.; Allen, W. D.; Schaefer, H. F., III *J. Chem. Phys.* **1998**, *108*, 9751.
(101) Allen, W. D.; East, A. L. L.; Császár, A. G. In *Structures and Conformations of Non-Rigid Molecules*; Laane, J., Dakkouri, M., van der Vecken, B., Oberhammer, H., Eds.; Kluwer: Dordrecht, 1993; pp 343−373.
(102) ACESII is a program product of the Quantum Theory Project, University of Florida. Authors: Stanton, J. F.; Gauss, J.; Watts, J. D.; Nooijen, M.; Oliphant, N.; Perera, S. A.; Szalay, P. G.; Lauderdale, W. J.; Gwaltney, S. R.; Beck, S.; Balková, A.; Bernholdt, D. E.; Baeck, K.-K.; Rozyczko, P.; Sekino, H.; Hober, C.; Bartlett, R. J. Integral packages included are VMOL (Almlöf, J., Helgaker, T., Jensen, H. J. Aa., Jørgensen, P., Olsen, J., Taylor, P. R.).
(103) *PSI 2.0.8*, Janssen, C. L.; Seidl, E. T.; Scuseria, G. E.; Hamilton, T. P.; Yamaguchi, Y.; Remington, R. B.; Xie, Y.; Vacek, G.; Sherrill, C. D.; Crawford, T. D.; Fermann, J. T.; Allen, W. D.; Brooks, B. R.; Fitzgerald, G. B.; Fox, D. J.; Gaw, J. F.; Handy, N. C.; Laidig, W. D.; Lee, T. J.; Pitzer, R. M.; Rice, J. E.; Saxe, P.; Scheiner, A. C.; Schaefer, H. F., III PSITECH Inc.: Watkinsville, Georgia, 30677, 1995.
(104) *Gaussian 94, Revision C*, Frisch, M. J.; Trucks, G. W.; Head-Gordon, M.; Gill, P. M. W.; Wong, M. W.; Foresman, J. B.; Johnson, B. G.; Schlegel, H. B.; Robb, M. A.; Replogle, E. S.; Gomperts, R.; Andres, J. L.; Raghavachari, K.; Binkley, J. S.; Gonzalez, C.; Martin, R. L.; Fox, D. J.; Defrees, D. J.; Baker, J.; Stewart, J. J. P.; Pople, J. A., Gaussian Inc.: Pittsburgh, PA, 1995.
(105) Supplementary material: http://zopyros.ccqc.uga.edu/ref_mat/supp_mat.html.
(106) Spielfiedel, A.; Feautrier, N.; Cossart-Magos, C.; Chambaud, G.; Rosmus, P.; Werner, H.-J.; Botschwina, P. *J. Chem. Phys.* **1992**, *97*, 8382.
(107) Robin, M. B. *Higher Excited States of Polyatomic Molecules, Vol. I*; Academic: New York, 1974.

(108) Robin, M. B. *Higher Excited States of Polyatomic Molecules, Vol. II*; Academic: New York, 1975.
(109) Robin, M. B. *Higher Excited States of Polyatomic Molecules, Vol. III*; Academic: New York, 1985.
(110) Buenker, R. J.; Peyerimhoff, S. D. *Chem. Rev.* **1974**, *74*, 127.
(111) Walsh, A. D. *J. Chem. Soc., Part III* **1953**, 2260 and articles which immediately follow.
(112) Herzberg, G. *Electronic Spectra and Electronic Structure of Polyatomic Molecules*; Van Nostrand Reinhold: New York, 1966.
(113) Lee, T. J.; Fox, D. J.; Schaefer, H. F., III; Pitzer, R. M. *J. Chem. Phys.* **1984**, *81*, 356.
(114) Eland, J. H. D. *Philos. Trans. R. Soc. London* **1970**, *268A*, 87.
(115) Wilsey, S.; Thomas, S. E.; Eland, J. H. D. *Chem. Phys.* **2000**, *258*, 21.
(116) Craddock, S.; Ebsworth, E. A. V.; Murdoch, J. D. *Faraday Trans. 2* **1972**, *68*, 86.
(117) Chang, D. P. *Theor. Chim. Acta* **1979**, *51*, 53.
(118) Cooley, J. W. *Math. Comput.* **1961**, *15*, 363.
(119) Numerov, B. *Publ. Obs. Central Ast.* **1933**, *2*, 188.
(120) *Mathematica, Version 2.2*, Wolfram Research, Inc.: Champaign, Illinois, 1993.
(121) Wolfram, S. *Mathematica: A System for Doing Mathematics by Computers*, 2nd ed.; Addison-Wesley: Redwood City, CA, 1991.
(122) Balasubramanian, K. *Relativistic Effects in Chemistry: Part A, Theory and Techniques*; Wiley: New York, 1997.
(123) Perera, S. A.; Bartlett, R. J. *Chem. Phys. Lett.* **1993**, *216*, 606.
(124) Kendall, R. A.; Dunning, T. H., Jr.; Harrison, R. J. *J. Chem. Phys.* **1992**, *96*, 6796.
(125) King, R. A.; Allen, W. D.; Ma, B.; Schaefer, H. F., III *Faraday Discuss. Chem. Soc.* **1998**, *110*, 23.
(126) Allen, W. D.; Schaefer, H. F., III *J. Chem. Phys.* **1988**, *89*, 329.
(127) Moore, C. B. *Faraday Discuss.* **1995**, *102*, 1.
(128) Green, W. H., Jr.; Moore, C. B.; Polik, W. F. *Annu. Rev. Phys. Chem.* **1992**, *43*, 591.
(129) Lovejoy, E. R.; Kim, S. K.; Moore, C. B. *Science* **1992**, *256*, 1541.
(130) Kim, S. K.; Lovejoy, E. R.; Moore, C. B. *J. Chem. Phys.* **1995**, *102*, 3202.
(131) Chen, I.-C.; Moore, C. B. *J. Phys. Chem.* **1990**, *94*, 263.
(132) Chen, I.-C.; Moore, C. B. *J. Phys. Chem.* **1990**, *94*, 269.
(133) Morgan, C. G.; Drabbels, M.; Wodtke, A. M. *J. Chem. Phys.* **1996**, *105*, 4550.
(134) Gezelter, J. D.; Miller, W. H. *J. Chem. Phys.* **1996**, *104*, 3546.
(135) Cui, Q.; Morokuma, K. *J. Chem. Phys.* **1997**, *107*, 4951.
(136) Allen, W. D.; Schaefer, H. F., III *J. Chem. Phys.* **1986**, *84*, 2212.
(137) Luna, A.; Mebel, A. M.; Morokuma, K. *J. Chem. Phys.* **1996**, *105*, 3187.